

0011
49944
P-44

Annual report of work progress on NASA grant NASW-4933

**"Plasma Properties and Magnetic Field Structure of the Solar Corona,
Based on Coordinated Max '91 Observations from SERTS,
the VLA, and Magnetographs"**

covering the period 12 July 1994 — 11 July 1995

PRINCIPAL INVESTIGATOR:

Dr. Jeffrey W. Brosius
Hughes STX Corporation
4400 Forbes Boulevard
Lanham, MD 20706-4392
Tel.: (301) 286-6200

(NASA-CR-198592) PLASMA PROPERTIES
AND MAGNETIC FIELD STRUCTURE OF THE
SOLAR CORONA, BASED ON COORDINATED
MAX 1991 OBSERVATIONS FROM SERTS,
THE VLA, AND MAGNETOGRAPHS Annual
Report, 12 Jul. 1994 - 11 Jul. 1995
(Hughes STX) 44 p

N95-27858

Unclass

63/92 0049944

1 Introduction

The purposes of this investigation are to use existing, calibrated, coaligned sets of coordinated multiwaveband observations of the Sun to determine the coronal magnetic field strength and structure (*i.e.*, derive coronal magnetograms), and interpret the collective observations in terms of a self-consistent model of the coronal plasma and magnetic field. This information is vital to understanding processes such as coronal heating, solar wind acceleration, pre-flare energy storage, and active region evolution. Understanding these processes is the central theme of Max '91, the NASA-supported series of solar observing campaigns under which the observations acquired for this work were obtained. Results from this project are directly relevant to NASA's SOHO mission, in that the EUV emission line diagnostic techniques evaluated and implemented in this analysis comprise test case studies of SOHO (particularly CDS) capabilities. It should be emphasized that the value of the SERTS data for this type of analysis depends critically upon the accuracy of the relative photometric calibration. This is measured at the Synchrotron Ultraviolet Radiation Facility (SURF-II) of the National Institute of Standards and Technology.

The observations were obtained with NASA/GSFC's Solar EUV Rocket Telescope and Spectrograph (SERTS), the Very Large Array (VLA), and magnetographs. When the proposal requesting NASA support for this project was submitted back in September of 1993, the quality of the data from the SERTS flight of 17 August 1993 was not yet known. The proposal stated, however, that if those data became available and were of sufficiently high quality, they would be analyzed in addition to the data from the 1991 flight. I have examined the data from the 1993 flight and found them to be of superior quality even to the data from the 1991 flight. I therefore decided to analyze data from both flights simultaneously.

I exploit the dependence of the coronal microwave emission upon the coronal magnetic field strength in order to calculate the coronal magnetic field. The technique is to establish the contributions to the microwave emission from the two main emission mechanisms: thermal bremsstrahlung and thermal gyroemission. This is done by using the EUV emission to determine values of the coronal plasma quantities needed to calculate the thermal bremsstrahlung contribution to the microwave emission. Once the microwave emission mechanism(s) are determined, the coronal magnetic field can be calculated. Because maps of coronal emissions originating in different height layers are available in both the EUV and microwave wavebands, I will derive three-dimensional models of the coronal plasma and magnetic field for each area observed which are consistent with all of the EUV spectra and spectroheliograms, as well as with the intensity and polarization maps at all of the microwave observing frequencies. Finally, a comparison of the coronal magnetic field derived from the coordinated multiwaveband observations with extrapolations from photospheric magnetograms will provide insight into the nature of the coronal magnetic field (potential or non-potential).

2 Achievements

Substantial progress, summarized in this section, was made toward successfully completing this research program. For brevity, the various accomplishments are bulletized in the following subsections. Overall progress toward the completion of the long-term, main goals is given in §2.1, specific short-term achievements are listed in §2.2, collaborations are discussed in §2.3, and deliverables

are enumerated in §2.4. As planned in the original proposal, the first year's effort under this grant placed heavy emphasis on plasma diagnostic techniques. This is immediately evident from the items listed below.

SERTS spectral data from both the 7 May 1991 and the 17 August 1993 flights were analyzed simultaneously. For each flight, digitized, calibrated spectral arrays were provided by Drs. Joseph Davila and Roger Thomas of the Laboratory for Astronomy and Solar Physics at NASA/GSFC. For the 1991 flight I selected appropriate portions of the slit and obtained averaged spectra for quiet Sun areas, areas along the edge of AR 6615, and areas above the limb. For the 1993 flight I similarly obtained averaged spectra for quiet Sun areas and for AR 7563.

2.1 Progress Toward Long-Term Goals

- Completed an assessment of various plasma diagnostic techniques, using the derived active region, quiet Sun, and off-limb averaged spectra. This analysis provides the groundwork necessary for ultimately deriving coronal magnetic fields, and is the subject of three presentations and two papers submitted for publication.
- Provided new physical insight into active region and quiet Sun coronal structures.
- Made recommendations for SOHO observations.
- Converted old FORTRAN code for microwave emission modeling to IDL; wrote new IDL software for developing three-dimensional models of coronal magnetic fields.

2.2 Short-Term Goals

- Plate flaws sought and removed from digitized SERTS data (20,000 x 80 arrays).
- Averaged spectra obtained for selected solar features.
- Background calculated and subtracted from each averaged spectrum.
- Spectra searched for emission line candidates.
- Emission line candidates (~ 100 per spectrum) fitted with Gaussian profiles.
- Lists of "real" emission lines compiled.
- Relative wavelength calibration verified by density- and temperature- insensitive ratios.
- Densities and temperatures derived from appropriate intensity ratios.
- Differential emission measure derived for active and quiet spectra.
- Revised existing, and wrote new, IDL software for various tasks. All software will be useful for analysis of data from future flights, at least one of which will be coordinated with SOHO for calibration purposes.

2.3 Collaborations

- Collaboration with Dr. B. C. Monsignori-Fossi, who provides extensive tables of line emissivities as functions of density and temperature. This collaboration is mutually beneficial because Dr. Monsignori-Fossi needs real solar spectra to test her differential emission measure code (written for analysis of SOHO observations), and I need the most up-to-date emissivity calculations available

in order both to test the SERTS calibration, and to perform density, temperature, and emission measure diagnostic calculations.

- Collaboration with Dr. Anand Bhatia, for purposes of improving our theoretical understanding of the Mg VIII ion.
- Useful discussions (although no formal collaboration as yet) with Dr. H. E. Mason and Mr. P. R. Young, for purposes of improving our understanding of the Fe XIII ion.

2.4 Finished Products

- One paper submitted to *The Astrophysical Journal*: “Measuring Active and Quiet Sun Coronal Plasma Properties with EUV Spectra from SERTS,” by J. W. Brosius, J. M. Davila, R. J. Thomas, and B. C. Monsignori-Fossi. (Appended to this document.)
- One paper submitted to the special SOHO issue of *Annales Geophysicae*: “Measuring Coronal Plasma Properties with EUV Spectra from SERTS: Implications for SOHO Observations,” by J. W. Brosius, J. M. Davila, R. J. Thomas, and B. C. Monsignori-Fossi.
- Presentations at three scientific meetings:
 - IAU Colloquium # 153, “Magnetodynamic Phenomena in the Solar Atmosphere – Prototypes of Stellar Magnetic Activity,” Makuhari near Tokyo, Japan, May 22 - 26, 1995;
 - “Eleventh Colloquium on UV and X-Ray Spectroscopy of Astrophysical and Laboratory Plasmas,” Nagoya, Japan, May 29 - June 2, 1995 (INVITED);
 - Twenty-Sixth Solar Physics Division Meeting, Memphis, TN, June 4 - 8, 1995.
- Provided EUV line lists which are being used in preparation for
 - TRACE (provided to Dr. Leon Golub)
 - SOLAR-B (provided to Dr. Hirohisa Hara).

3 Analysis

Some of the key results from “Measuring Active and Quiet Sun Coronal Plasma Properties with EUV Spectra from SERTS” (Paper I), submitted to ApJ and appended to the end of this document, are summarized below:

- The derived active region densities range from $10^{7.6}$ to $10^{10.4} \text{ cm}^{-3}$, and quiet Sun densities range from $10^{7.4}$ to $10^{10.1} \text{ cm}^{-3}$.
- Widely differing densities within each solar feature were derived from the many available line ratios of Fe XIII, suggesting the presence of multiple density structures.
- It is advisable that data sets obtained with the SOHO spectrometers include as many different density diagnostic ratios as possible, for purposes of cross-checking and to avoid over-reliance upon potentially “inappropriate” ratios.
- The “hottest” ion seen in the quiet Sun spectra is Fe XVI ($\log T_{max} = 6.4$); the active region spectra show emission from Ni XVIII and Fe XVII ($\log T_{max} = 6.5$ and 6.7 , respectively).
- Active region temperatures derived from ratios of lines from different ionization stages of iron range from 1.26×10^6 to $5.25 \times 10^6 \text{ K}$, and quiet Sun temperatures range from 1.17×10^6 to $2.95 \times 10^6 \text{ K}$.

- For line intensity ratios which include lines from only Fe X, XI, XII, and XIII, the active region and quiet Sun temperatures are not statistically significantly different. When lines from Fe XIV, XV, and XVI are included, the active region temperatures are statistically significantly greater than the quiet Sun temperatures.
- Differential emission measure distributions were constructed, and can be used for the theoretical microwave emission calculations.

4 Statement of Work

For the second year of this project, the emphasis will shift from plasma diagnostic techniques to analysis of microwave emission mechanisms and derivation of coronal magnetic fields and overall three-dimensional coronal structures. I will use the differential emission measure results to help calculate the thermal bremsstrahlung microwave emission, and proceed as originally described in my proposal. It should be pointed out that use of the DEM is a different but better approach than the one originally planned. Briefly, I will obtain one-dimensional scans and two-dimensional maps of coronal plasma properties using the emission line diagnostic techniques described in Paper I. I will derive emission measure distributions for each pixel where practicable, or, more likely, scale the emission measure distribution derived from the averaged spectra according to the local (pixel) intensities of selected emission lines. With this information I will derive maps and/or scans of the thermal bremsstrahlung microwave emission for comparison with the observed microwave emission. This comparison will indicate the presence or absence of thermal gyroemission, and the presence or absence of cool absorbing plasma. This information, combined with existing and developing IDL software, will enable me to deduce maps of the coronal magnetic field. Because of the availability of multiple microwave frequencies, I will be able to obtain magnetic field maps for several different height regimes. This, in turn, will lead to three-dimensional models of the coronal plasma and magnetic field which are consistent with all of the available data. Finally, comparisons will be made between the magnetic field derived by the above method, and potential field extrapolations. Results will be presented at scientific meetings and submitted to a refereed journal for publication.

SECTION B - SUPPLIES OR SERVICES AND PRICES/COSTS

B.1 ESTIMATED COST AND FIXED FEE. (DEC 1991) 1852.216-74

The estimated cost of this contract is \$43,982 exclusive of the fixed fee of \$2,199. The total estimated cost and fixed fee is \$46,181.

The contract will be increased, when the option(s) to extend the term of the contract are exercised as stipulated in Section I of this contract, by the amount indicated below.

	<u>Estimated Cost</u>	<u>Fixed Fee</u>	<u>Total Est. CPFF</u>
Basic Contract	\$43,982	\$2,199	\$46,181
Option Period I	\$46,521	\$2,326	\$48,847

(End of clause)

SECTION C - DESCRIPTION/SPECIFICATIONS/WORK STATEMENT

The contractor shall provide all the necessary personnel, facilities, equipment, material and services to accomplish the Contractor's proposal entitled "Plasma Properties and Magnetic Field Structure of the Solar Corona, Based on Coordinated Max '91 Observations from SERTS, the VLA and Magnetographs" dated September 1, 1993 which is hereby incorporated by reference. All work performed under this contract shall be in accordance with this proposal

SECTION D - PACKAGING AND MARKING

{End of Section}

SECTION E - INSPECTION AND ACCEPTANCE

52.246-9 INSPECTION OF RESEARCH AND DEVELOPMENT (SHORT FORM) APR 1984

SECTION F - DELIVERIES OR PERFORMANCE

52.212-13 STOP-WORK ORDER AUG 1989
-- ALTERNATE I (APR 1984)

1852.212-70 NOTICE OF DELAY DEC 1988

F.1 DELIVERY SCHEDULE. (DEC 1988) 1852.212-73

Measuring Active and Quiet Sun
Coronal Plasma Properties
with EUV Spectra from SERTS

Jeffrey W. Brosius¹, Joseph M. Davila, Roger J. Thomas
Code 682.1, NASA/Goddard Space Flight Center, Greenbelt, MD 20771

and

Brunella C. Monsignori-Fossi
Osservatorio Astrofisico di Arcetri, Florence, Italy

Submitted to *The Astrophysical Journal*
April 25, 1995

Running title: Active and Quiet Sun EUV Spectra from SERTS

¹ also Hughes STX Corporation, 4400 Forbes Blvd., Lanham, MD 20706

Abstract

We obtained high-resolution extreme-ultraviolet (EUV) spectra of solar active regions, quiet Sun areas, and off-limb areas during 1991 May 7 and 1993 August 17 flights of NASA/Goddard Space Flight Center's Solar EUV Rocket Telescope and Spectrograph (SERTS). Emission lines from the eight ionization stages of iron between Fe^{+9} (Fe X) and Fe^{+16} (Fe XVII) are included in the observed bandpass. Intensity ratios among various lines originating in a common stage of ionization provide either measurements of coronal electron density or — if the ratio is density insensitive — verification of the relative wavelength calibration. Active region densities ranging from $10^{7.6}$ to $10^{10.4} \text{ cm}^{-3}$, and quiet Sun densities ranging from $10^{7.4}$ to $10^{10.1} \text{ cm}^{-3}$, were obtained. Widely differing densities in each solar feature were derived from the many available line ratios of Fe XIII; however, each individual line pair yielded comparable densities for all features, with the active region densities exceeding the quiet Sun densities. This suggests the presence of multidensity structures in the active regions, quiet Sun areas, and off-limb areas observed. It is advisable that observations obtained with the spectrometers aboard the Solar and Heliospheric Observatory (SOHO) spacecraft include as many different density diagnostic ratios as possible, for purposes of cross-checking and to eliminate over-reliance upon potentially “inappropriate” ratios. Intensity ratios among lines originating in different ionization stages of iron yield measurements of coronal electron temperature in the isothermal approximation. The line ratios yielded temperatures ranging from 1.26×10^6 to $5.25 \times 10^6 \text{ K}$ for the active regions, and 1.17×10^6 to $2.95 \times 10^6 \text{ K}$ for the quiet Sun. Fe XVII emission, detected in the active regions but not in the quiet areas, accounts for the higher derived active region temperatures. The derived active region and quiet Sun temperatures are not statistically significantly different for line intensity ratios which involve only Fe X through Fe XIII; however, the derived active region temperatures are statistically significantly greater than their quiet Sun counterparts for ratios which include lines from Fe XIV through Fe XVI. This similarity in derived temperatures suggests the presence of similar multithermal structures in all of the areas observed, with the active regions harboring hotter material. Differential emission measure distributions were constructed for the active region and quiet Sun observations obtained during both flights.

1 Introduction

Reliable measurements of quantities such as density, temperature, emission measure, and magnetic fields in solar coronal structures are essential for understanding those structures and the processes occurring in them. Such processes include coronal heating, flare energy storage, and active region evolution. Typical active region structures are characterized by ranges in parameter values, *e.g.*, high and low density plasmas may be intermixed, and the temperature and magnetic field strength vary with height as well as with position across the disk. In general the more extensively one samples the range of parameter values, the more completely one can understand the observed structures.

Well-determined values of the temperature and emission measure are necessary, for example, for a meaningful comparison with coordinated microwave observations to yield the coronal magnetic field (*e.g.*, Brosius *et al.* 1993, Schmelz *et al.* 1994, and references therein; Gary & Hurford 1994). During the Solar Maximum Mission era, coronal temperatures were obtained from X-Ray Polychromator observations by comparing measured intensity ratios of emission lines originating in ions of different elements with their corresponding temperature-dependent theoretical response functions. This technique worked reasonably well (*e.g.*, Brosius *et al.* 1992; Schmelz *et al.* 1992, 1994; Nitta *et al.* 1991; Saba & Strong 1991), but can be hampered by uncertainties in the coronal elemental abundances (Falconer 1994; Meyer 1993; Falconer, Davila, & Thomas 1993; Saba & Strong 1993; Schmelz, Strong, & Lemen 1993; Widing & Feldman 1993; Feldman 1992). This problem is eliminated by using emission lines from different stages of ionization of the same element, and is one topic of the present study. More recently, coronal temperatures have been obtained from the Soft X-ray Telescope aboard the *Yohkoh* spacecraft by comparing the ratios of broad-band coronal emission, viewed through pairs of filters, with their corresponding temperature-dependent theoretical response functions. *Yohkoh* is well known to be particularly sensitive to relatively hot plasma (see, *e.g.*, Fig. 9 in Tsuneta *et al.* 1991), and consistently yields temperatures in excess of 4×10^6 K. Taken by themselves, such observations may be misleading because they are biased toward the higher values. However, when combined with coordinated multiwaveband observations sensitive to lower temperatures (*e.g.*, Klimchuk & Gary 1995, Aschwanden *et al.* 1995), they provide wider coverage of parameter space.

In the present study we describe methods of deriving coronal temperature, density, and differential emission measure from EUV spectra covering the wavelength range from 300 to 420 Å. Earlier solar observations in this wavelength range, obtained with the Harvard scanning spectrometer on OSO-6 (Dupree *et al.* 1973) and with the EUV spectrometer-spectroheliometer on Skylab (Vernazza & Reeves 1978), had such coarse spectral resolution ($\sim 1.6 - 1.8$ Å) to preclude accurate determinations of coronal plasma properties from line ratio measurements. However, their spatial resolution was adequate to separate active from quiet Sun areas, and enabled them to suggest that temperatures at least as high as 2.5×10^6 K occur in quiet Sun areas (Vernazza & Reeves 1978), and to find that the higher the temperature of line formation, the greater the enhancement of active region compared to quiet Sun intensity (Dupree 1973). Behring *et al.* (1976) obtained spectra with 0.06 Å spectral resolution during two sounding rocket flights, and provided many line identifications which were used by Thomas & Neupert (1994) as well as in the present work. However, those spectra were acquired from full-Sun observations, and so provide no information about distinct features on the Sun. Furthermore, the relative line intensities were only approximately calibrated, rendering line intensity ratio measurements inaccurate. Thus, to date, the observations described in the present work represent the best-suited EUV observations for diagnosing coronal

plasma conditions.

We obtained spectra of AR 7563 and of quiet Sun areas on 1993 August 17, and of AR 6615, quiet Sun areas, and off-limb areas on 7 May 1991 with NASA/Goddard Space Flight Center's Solar EUV Rocket Telescope and Spectrograph (SERTS). Emission lines formed at temperatures ranging from 1×10^5 K (He II) to 5×10^6 K (Fe XVII) are available, providing extensive temperature coverage. Furthermore, numerous density-sensitive line pairs are also available, enabling the direct measurement of plasma density. Since the Coronal Diagnostic Spectrometer (CDS) on the SOHO spacecraft will be capable of observing the Sun in many of the emission lines considered here, the analysis techniques described below are applicable to CDS/SOHO observations. Section 2 describes the SERTS observations, §3 discusses the spectra and corresponding lists of line intensities, §4 presents methods of deriving coronal plasma properties, and §5 summarizes our conclusions.

2 SERTS Observations

The Solar EUV Rocket Telescope and Spectrograph (SERTS) instrument incorporates a grazing-incidence Wolter 2 telescope to form a real image of the Sun on the entrance aperture of a quasi-stigmatic spectrograph. An image of this aperture is then formed on the spectrograph grating, which ultimately reimages it simultaneously in each dispersed wavelength on EUV-sensitive photographic film. The spectrograph entrance aperture was designed so that both spectra and spectroheliograms can be obtained simultaneously: spectra are obtained along a narrow $4'.9$ -long slit connecting two rectangular lobes within which the spectroheliograms are imaged. The upper lobe covers a $4'.8 \times 8'.2$ area on the Sun, and the lower one covers a $4'.8 \times 7'.6$ area. The spatial resolution is $\sim 7''$, and the spectral resolution is < 75 mÅ. By adjusting the pointing of the instrument during its flight, both images and spectra can be obtained for the same portion of the Sun. A detailed description of the instrument is given by Neupert *et al.* (1992b).

SERTS was launched on a Terrier-boosted Black Brant rocket from White Sands, NM, at 1805 UT on 7 May 1991 and on 17 August 1993. It reached a maximum altitude of 327 km during both flights, and acquired spectrographic data from 1806 to 1813 UT. The 1991 flight was the first of a multilayer coated diffraction grating (Davila *et al.* 1992; Keski-Kuha, Thomas, & Davila 1992). This multilayer coating enhanced the instrumental sensitivity over that of the uncoated grating for wavelengths between 250 and 350 Å (Thomas *et al.* 1991). The same instrument was flown on both occasions and it performed well, obtaining spectra and spectroheliograms in the wavelength range of 235 to 450 Å. During each flight we obtained four different exposures in each of two different pointing positions. This ensured the availability of optimally-exposed spectral lines and spectroheliograms for both strong and weak spectral features, and provided the information needed to determine the film density *vs.* log energy (D-log E) relation (Thompson *et al.* 1993). The data were recorded on Eastman Kodak 101-07 EUV-sensitive photographic film, and digitized with a Perkin-Elmer microdensitometer. The spectral dimension of the resulting two-dimensional arrays is perpendicular to the length of the slit, and the spatial dimension is parallel to it. Following Thomas & Neupert (1994), corrections for the effects of atmospheric extinction at rocket altitudes were made for each exposure and incorporated into our calculations of the film response and overall instrumental sensitivity. The procedures for establishing the wavelength scale and the photometric calibration are also similar to those described in Thomas & Neupert (1994) for the SERTS flight of

1989 (which used an uncoated grating). Relative line intensities are accurate to better than 20% at wavelengths above 300 Å but are considerably worse at wavelengths below 300 Å. The absolute photometric scale is estimated to be accurate to better than a factor of 2.

In this paper we concentrate only on the spectral data, obtained with the slit portion of the entrance aperture. We present three spectra from the 1991 flight, and two from 1993. In each case, the spectra were averaged along the portion of the slit which passed through a designated feature on the Sun; thus, we averaged the spectral information over the spatial dimension. For the 1991 flight, an active region spectrum was obtained from the 159'' portion of the slit which grazed AR 6615 (S10W30), a quiet Sun spectrum was obtained from a 132'' portion of the slit, and an off-limb spectrum was obtained from a 53'' portion of the slit above the limb. The 1991 active region spectrum was obtained in the second pointing position, and the quiet Sun and off-limb spectra were obtained in the first. For the 1993 flight, an active region spectrum was obtained from the 163'' portion of the slit which bisected AR 7563 (S01W15), and the quiet Sun spectrum was obtained from the entire length of the slit (282'') which passed through quiet Sun areas. The 1993 active region spectrum was obtained in the first pointing position, and the quiet Sun spectrum in the second.

Because of the known relative calibration problem for wavelengths shorter than 300 Å, we present here spectra and emission lines only for wavelengths greater than 300 Å. Note that this calibration problem does not affect the results of Brosius *et al.* (1993) because, in that work, the Fe XV 284 Å intensity was corrected by a factor which placed it in correct proportion to other Fe XV lines.

3 Spectra

The procedure described below was followed to obtain the spectra and line lists given in this paper. First, plate flaws such as bright dots and streaks were removed from the digitized data by carefully examining each two-dimensional spectral array, and replacing notable flaws with uncontaminated local averages. After the data were cleaned, they were averaged along appropriate portions of the slit to obtain spectra from the five distinct solar features described above. Each averaged spectrum was found to display an obvious background level (due to film fog, scattered light, and actual solar continuum) which varies with wavelength. The background was determined for each spectrum by fitting every emission line candidate with a gaussian profile superimposed on a quadratic substrate, and replacing the line candidates with their respective local substrate values. After every significant emission line candidate was removed, all that remained of the original spectrum was its background. This background was then smoothed and subtracted from the original spectrum to obtain the final emission line spectrum.

Figures 1 and 2 show active region and quiet Sun spectra from the 1993 flight, and Figures 3 - 5 show active region, quiet Sun, and off-limb spectra from the 1991 flight. In each case the horizontal scale is the wavelength in Å, and the vertical scale is the spectral intensity in $\text{erg cm}^{-2} \text{s}^{-1} \text{sr}^{-1} \text{Å}^{-1}$. Each of these spectra has been smoothed. The 1993 active region spectrum shown in Figure 1 was obtained from a 99.4 s exposure acquired in the first pointing position. The emission lines of He II at 303.8 Å and Fe XVI at 335.4 Å are saturated in this spectrum (*i.e.*, their respective film

densities lie outside the linear portion of the film's D-log E relation), but are well-exposed in a 20.2 s exposure obtained in the same pointing position. The 1993 quiet Sun spectrum shown in Figure 2 was obtained from a 202.3 s exposure acquired in the second pointing position. Here the emission line of only He II at 303.8 Å is saturated, but it is well-exposed in a 40.3 s exposure from the same pointing position. The 1991 active region spectrum shown in Figure 4 was obtained from a 202.3 s exposure acquired in the second pointing position. Both He II at 303.8 Å and Fe XVI at 335.4 Å are saturated in this spectrum, but they are well exposed in a 40.3 s exposure from the same pointing position. The 1991 quiet Sun and off-limb spectra shown in Figures 4 and 5 were obtained from a 99.4 s exposure acquired in the first pointing position. None of the lines are saturated in these spectra. Notice that effects of the multilayer passband edge are evident in all five spectra by the apparent increase in noise level above ~ 350 Å; indeed, the grating efficiency outside the multilayer passband is actually less than what it would be in the uncoated case.

Several differences among the spectra are readily visible, some attributable to observational technique and others to intrinsic spectral diversity. Notice that the 1993 quiet Sun spectrum has the lowest noise level of all five spectra. This seems counter-intuitive because the quiet Sun emission lines are weaker than their active region counterparts, but it occurs because both the exposure duration and the portion of the slit along which the spectrum was averaged were greater for the quiet Sun than for the active region. The noise level in the 1991 active region spectrum is greater than that of the 1993 quiet Sun spectrum because, although both spectra were obtained with 202.3 s exposures, the 1991 spectrum was averaged along a smaller section of the slit. The 1991 off-limb spectrum is the noisiest of all five spectra because it was obtained from both the shortest duration exposure and the smallest slit segment. Note also that the Fe XVII line at 350.5 Å, easily seen in the 1991 active region spectrum and weak but visible in the 1993 active region spectrum and the 1991 off-limb spectrum, is absent from the quiet Sun spectra (despite the long exposure and the whole-slit average used to obtain the 1993 quiet Sun spectrum). This indicates, as expected, that hotter plasma exists in active regions than in quiet Sun areas. This will be better quantified in the discussion which follows.

Lists of emission line candidate wavelengths were obtained by searching the unsmoothed, background-corrected spectra for features in which the peak intensity exceeded three times the standard deviation of the local background noise. A few weaker candidates known to correspond to previously observed emission lines were also selected, but no attempt was made to compile as extensive a list as that given by Thomas & Neupert (1994). Each identified line candidate in the unsmoothed, background-corrected spectra was then fitted to a Gaussian profile superimposed on a zero-valued local background. The resulting individual Gaussian profiles were visually examined, and either accepted as real spectral lines or discarded as noise depending upon the line width and overall quality of the fit. Since 50 mÅ represents the smallest instrumental width (full width at half-maximum) in these observations, line candidates narrower than this were typically omitted. (A few exceptions are included in the tables below.) In addition, some line candidates were sufficiently noisy to preclude the fitting of a Gaussian profile which truly resembles the spectral data. Such candidates were also discarded. The remaining candidates were accepted as real solar emission lines. Lists of the lines extracted in this way from each of the five averaged solar spectra are given in Tables 1 - 5.

Each table provides the identification (after Thomas & Neupert 1994) of the ion responsible for the emission observed at each wavelength (in Å). Each table also provides the integrated intensity and its associated uncertainty (both in $\text{erg cm}^{-2} \text{ s}^{-1} \text{ sr}^{-1}$), and the line width (full width at half

maximun) and its associated uncertainty (both in mÅ). The wavelengths, intensities, widths, and uncertainties were all calculated from the Gaussian profile fit parameters, and their formal standard deviations, by methods similar to those described in Thomas & Neupert (1994). Wavelengths were determined by inserting the pixel coordinates of the centroids of the fitted Gaussians into a wavelength conversion function which was derived from laboratory measurements. Uncertainties in the derived wavelengths, not listed in the tables, originate from a variety of sources and are expected to be several 10's of mÅ for most lines. The wavelength conversion function itself contributes the majority of this uncertainty, but additional errors arise from the following. The centroid of the He II fitted Gaussian in each spectrum was assumed to lie at a wavelength of exactly 303.782 Å, which means that any uncertainty associated with the determination of the location of this centroid (typically < 1 mÅ) is propagated to the measured wavelengths of all the other lines. The uncertainties associated with the individual measurements of the centroid locations of all of the other lines are typically < 10 mÅ, the largest values being associated with the weakest, noisiest lines. Although Doppler shifts due to mass motions were found to produce wavelength shifts in Mg IX 368.1 Å over a short segment of the 1989 SERTS slit (Neupert *et al.* 1992a), such motions are more likely to contribute to profile broadening in these averaged spectra.

The values of the integrated intensity I and the full width at half maximum FWHM were obtained from the amplitude A and the Gaussian width W of each Gaussian profile by

$$I = (2\pi)^{1/2} AW \quad (1)$$

and

$$FWHM = 2(2\ln 2)^{1/2}W. \quad (2)$$

The associated uncertainties are given by

$$\sigma_I = (2\pi)^{1/2}[W^2(\sigma_A^2 + u_A^2) + A^2(\sigma_W^2 + u_W^2)]^{1/2} \quad (3)$$

and

$$\sigma_{FWHM} = 2(2\ln 2)^{1/2}(\sigma_W^2 + u_W^2)^{1/2}, \quad (4)$$

where $u_A = 0.1A$ and $u_W = 0.05W$ are estimated uncertainties due to photographic D-log E conversion. Most of the lines listed in each table were derived from the longest exposures available. However, the intensities of the lines which were saturated in the longest exposure were obtained from the next longest exposure. The measured line intensities were placed onto an absolute scale such that the sum I_{sum} of the He II 303.8 Å and Si XI 303.3 Å quiet Sun intensities agrees with the results of Mango *et al.* (1978), in which I_{sum} is 7115 erg cm⁻² s⁻¹ sr⁻¹ at disk center and brightens by ~ 30% toward the limb.

A number of emission line intensity ratios are either insensitive to or nearly insensitive to the density and temperature of the emitting plasma (*e.g.*, Neupert & Kastner 1983). A post-flight calibration verification was performed on the SERTS data by comparing measured values of such line intensity ratios with their corresponding theoretical values. Results of this comparison are shown in Table 6. Values derived from the 1989 active region spectrum of Thomas & Neupert (1994) are included for comparison. The uncertainties listed for some of the theoretical values are due to the small variations in the intensity ratios with density and/or temperature. It should be pointed out that uncertainties as large as 20 – 30 % are expected for some of the theoretical line emissivities, which would translate into even larger uncertainties in the theoretical values of the line intensity ratios. Notice, however, that most of the measured line intensity ratios agree with their

corresponding theoretical values within or close to within their tabulated errors, and that all of them agree within a factor ~ 2 . This demonstrates the accuracy of the SERTS relative wavelength calibration, confirms the general validity of the atomic physics calculations, and indicates the soundness of our background correction and Gaussian fitting techniques. Better agreement between the theoretical and the measured values is obtained for the 1993 than for the 1991 flight. This is possibly due to the fact that many more flaws were found in the 1991 data than in the 1993 data.

4 Results

The lists of emission lines that we have derived for solar active regions, quiet Sun, and off-limb areas are not exhaustive: additional weak lines could certainly be extracted, as well as blended lines separated, for each of the spectra. However, the present lists of predominant emission lines can be used to note similarities and differences among the various solar features, as well as to determine properties of the emitting plasmas.

All of the lists have numerous emission lines in common, including lines from Fe X ($\log T_{max} = 6.0$) through Fe XVI (6.4), Si VIII (5.9) through Si XI (6.2), Mg VIII (5.9) and IX (6.0), Cr XIII (6.2), Al X (6.1), and He II (4.7). The temperature logarithm, $\log T_{max}$, is that of maximum line emissivity. Several lines of Ne V (5.5) and VI (5.6) are found also in the active region and quiet Sun spectra. Two major differences between the active region and the quiet Sun spectra are noticeable. First, only the active regions show emission from ions with $\log T_{max} > 6.4$, namely, Ni XVIII (6.5) and Fe XVII (6.7). Emission lines from those ions are not found in the quiet Sun spectra, even in the long duration, whole-slit-length quiet Sun exposure from the 1993 flight. Second, the active region emission line intensities are more enhanced compared to their quiet Sun counterparts for higher ionization stages than for lower ones. This is shown in Figure 6 for the seven ionization stages of iron between X and XVI. Similar ratios of the Si and Mg lines yield comparable results.

An interesting facet of the 1991 observations is that the quiet Sun Fe X through Fe XIII intensities are actually greater than their corresponding active region values (see Figure 6). The explanation for this is not immediately apparent, although several possibilities exist. First, although there is definitely no active region anywhere along the slit in the pointing position from which the 1991 quiet Sun spectrum was derived, the He I 10830 Å image obtained with the NASA/NSO Spectromagnetograph at Kitt Peak does indeed show somewhat enhanced activity compared to that of the area from which the 1993 quiet Sun spectrum was derived. Most of the 1991 quiet Sun line intensities are enhanced over their 1993 quiet Sun values by factors of 2 – 3 (some by smaller values), suggesting a more energetic quiet state. However, as described below, each temperature-sensitive line intensity ratio yields equal (within the uncertainties) 1991 and 1993 quiet Sun temperatures (see Table 10), and the derived differential emission measure distributions are also quite similar (see Figure 9). Second, as mentioned above, the 1991 active region spectrum was obtained from a pointing position in which the slit *grazed*, but did not pass directly through, an active region. Thus it may simply be that the 1991 active region spectrum, although certainly obtained from an area of enhanced activity, is not fully an *active region* spectrum.

We derived densities for the observed solar features from ratios of emission lines which originate in a common ionization stage of iron. Densities were derived by cubic spline interpolation on ratios

of the line emissivity values tabulated by Monsignori-Fossi & Landini (1995a), evaluated at the temperature of maximum line emissivity, T_{max} . The temperature at which the interpolation is performed does not significantly affect the derived densities (unless, in some cases, T is far from T_{max} , which is not the case in the present work). Table 7 lists values of densities derived from the spectra of the different solar features acquired during the 1993 and 1991 SERTS flights, and includes values derived from the 1989 active region spectrum (Thomas & Neupert 1994) for comparison. The quoted uncertainties are due to intensity measurement uncertainties only. Note that the line intensity ratio of Fe XIII 318.1/320.8 yields a double-valued solution. All of the single-solution line intensity ratios yield greater active region than quiet Sun densities, although some of the derived active region and quiet Sun densities are not statistically significantly different within their calculated uncertainties.

Note especially the scatter in density obtained from the lines of Fe XIII for every solar feature. This scatter is unlikely to be attributed to errors in the relative wavelength calibration because that calibration has been confirmed by density- and temperature-insensitive line intensity ratios; it therefore appears to be a real solar phenomenon. Similar such scatter within each of several ionization stages of iron was noted for the 1989 SERTS data by Brickhouse, Raymond, & Smith (1995), who suggested that it could be attributed to multidensity structures along the line of sight. Key to this explanation is the fact that different emission lines, even for a given ion, are favored by different density regimes (see, *e.g.*, Doschek 1984). Observational support for this explanation derives from the fact that the Fe XIII 320.8/359.7 line intensity ratio consistently yields the lowest density in each available spectrum, while the 359.8/359.7 ratio consistently yields the highest. The other three non-double-valued ratios all yield intermediate results. This similarity in derived densities among different solar features suggests that individual line intensity ratios favor selected density ranges. It further suggests that similar mixtures of multiple coronal densities occur in active regions, quiet Sun areas, and off-limb areas. There is, however, at present no apparent explanation as to why the 320.8/359.7 ratio should consistently favor lower densities.

It bears repeating that uncertainties as large as $\sim 20 - 30\%$ are expected for at least some of the theoretical emissivities used in the present analysis. Further, the largest uncertainties are expected for the higher ionic transition levels. In the case of Fe XIII, for example, the upper and lower levels for the 348.2, 359.7, and 320.8 Å lines are 7 to 1, 8 to 2, and 12 to 3, respectively. Thus, Young & Mason (1995) ascribe greater reliability to the 359.7/348.2 and 320.8/348.2 Fe XIII ratios than to any other Fe XIII ratios. We conclude that, until the density diagnostic issue is satisfactorily settled once and for all, it is advisable for the SOHO spectrometers to collect as many density diagnostic ratios as possible during any given observation. This will ensure the capability of density diagnostic cross-checking, and will reduce the possibility of an interpretation which is biased by any “inappropriate” individual ratio.

We derived temperatures for the observed solar features from ratios of emission lines which originate in different ionization stages of iron. This was done by obtaining polynomial fits to the logarithm of the temperature T as a function of the logarithm of the emissivity ratio R for selected line pairs:

$$\log T = a_0 + a_1(\log R) + a_2(\log R)^2 + a_3(\log R)^3. \quad (5)$$

We again used the emissivity calculations of Monsignori-Fossi & Landini (1995a), which incorporate the ionization equilibrium calculations of Arnaud & Raymond (1992). Significant departures from ionization balance are not expected for the relatively quiescent regions analyzed in this paper.

Two functions were obtained for each line pair, one assuming a density of 10^9 cm^{-3} , and one assuming 10^{10} cm^{-3} . The coefficients a_0, a_1, a_2, a_3 are listed for each function in Tables 8 and 9. The difference between the temperatures calculated from these two functions for a given line pair provides the temperature uncertainty associated with plasma density uncertainties (although an admitted shortcoming is that this assumes a uniformly dense plasma). Table 10 lists temperature values derived from 17 different iron ion ratios. These values are the averages of their respective values calculated for densities of 10^9 and 10^{10} cm^{-3} . The error bars, which include contributions due to uncertainties in both plasma density as well as line intensities, bracket the temperatures calculated for densities of both 10^9 and 10^{10} cm^{-3} . Uncertainties in the derived temperatures due to uncertainties in the polynomial fits are negligible (more than an order of magnitude smaller than the uncertainties listed in Table 10). For reference we give the temperature logarithms for which each ionization stage of iron has its respective maximum emissivity: XVII (6.7), XVI (6.4), XV (6.3), XIV (6.3), XIII (6.2), XII (6.1), XI (6.1), X (6.0).

The mere presence of Fe XVII emission in the active region spectra, and its absence from the quiet Sun spectra, indicates that there is hotter plasma in the active regions than in the quiet Sun areas. However, The derived active region and quiet Sun temperatures are not statistically significantly different (judging from the uncertainties) as long as the ratios are restricted to lines from Fe X through Fe XIII. For ratios which include lines from among Fe XIV, XV, and XVI, the active region temperatures are statistically significantly greater than their quiet Sun counterparts. From the table, it is evident that there is an overall decrease in derived temperature for ratios involving increasingly lower stages of ionization. However, intensity ratios involving emission lines from only Fe X through Fe XIII yield extremely consistent values. This suggests the presence of a relatively uniform-temperature plasma, with $\log T \sim 6.13$. Brosius *et al.* (1994) found, for a limited segment of the 1991 active region slit using emission lines from only Fe XIII – XVI, that temperatures derived from emission lines originating in non-adjacent stages of ionization yielded consistent values. A similar consistency among temperatures derived from such ratios is also found in this work, although at slightly lower temperatures. Because temperatures derived in the present study are obtained from more accurate line emissivity calculations, as well as from less noisy averaged spectra (rather than from individual pixels), they are more reliable than the values obtained in the earlier work. The similarity in derived temperatures among the active regions, quiet sun areas, and off-limb areas indicates the presence of similar multithermal structures in all of these features.

Since each solar feature observed by SERTS manifests variety in its plasma density and temperature, it is useful to know the temperature distribution of emitting material within each feature. Such information is obtained from a differential emission measure (DEM) analysis. The DEM of a given solar feature can be empirically derived as a function of the temperature ($f(T)$) by combining measured spectral line intensities with their corresponding emissivities per unit emission measure (generally known as the contribution function). The numerical procedure used to evaluate the DEM in this work was developed in preparation for the SOHO mission (Monsignori-Fossi & Landini 1991, 1994b, 1995b), and has been applied to analyses of active stars observed by the Extreme Ultra-Violet Explorer (EUVE) (Landini & Monsignori-Fossi 1993; Monsignori-Fossi & Landini 1994a; Monsignori-Fossi *et al.* 1995a, 1995b). The method consists of an iterative procedure in which $f(T)$ is described by a cubic spline function through a small number of n mesh points ($f(T_i)$, $i=1, \dots, n$), and the $f(T_i)$ are varied until the best fit with the observations is obtained. This method assures only positive solutions, and allows control of the smoothness of the solution through the number of mesh points. In order to obtain the best $f(T)$ distribution it is important to select spectral lines which are relatively density-insensitive, and which cover a wide range in temperature. Large inde-

terminations may occur in temperature intervals where poor constraints are given by the available observations.

Results of the DEM analysis for the active and quiet regions observed by SERTS in 1991 and 1993 are given in Figures 7 and 8. All of the curves were derived by fitting available lines of Fe, Ne, Mg, Si, Al, and Ni, assuming the elemental abundances of Feldman (1992). Different symbols are used for the different elements in each figure. The x-coordinate of each symbol indicates the location of the temperature at which the product of the DEM and contribution function is maximized; this is the temperature of the maximum contribution to the line emission. The y-coordinate is the product of the DEM and the ratio of the observed to the predicted intensities. The error bars on each symbol represent the uncertainties attributed to intensity measurements only. All of the curves show an extremum between $\log T = 6.1$ and 6.2 , which is consistent with the temperatures derived from ratios of lines of Fe X through XIII. The quiet Sun differential emission measures drop off sharply for higher temperatures, but the active region DEMs show a second extremum between $\log T \sim 6.7$ and 6.8 . This is consistent with our finding that line ratio temperatures indicate the presence of hotter plasma in the active regions than in the quiet Sun areas. Further, the high-temperature DEM peak exceeds the low-temperature DEM peak for the 1991 active region, but the situation is reversed for the 1993 active region. This is consistent with our finding that the 1991 active region yields a greater maximum temperature (5.25×10^6 K) than does the 1993 active region (4.07×10^6 K). This temperature difference may be a manifestation of the different levels of activity in the two regions: the photospheric longitudinal magnetic field measured with the NASA/NSO Spectromagnetograph at Kitt Peak (Jones *et al.* 1992) indicates that the maximum magnetic field strength in the 1991 active region is a factor of four greater than that in the 1993 active region.

5 Conclusions

We obtained spectra of solar active regions, quiet Sun areas, and off-limb areas from two flights of the SERTS instrument. Density- and temperature-insensitive line intensity ratios verify the relative wavelength calibration of the instrument. The densities derived from selected line intensity ratios are typically greater in the active regions than in the quiet Sun areas, although in a few cases the differences are not statistically significant. Densities derived for each observed feature from intensity ratios among the numerous emission lines of Fe XIII are scattered over nearly two orders of magnitude; however, each individual ratio consistently yields either the highest, or the lowest, or an intermediate value of the density for all of the observed features. This suggests the presence of multidensity structures in all of the features observed, and calls into question the measurement of unique densities in such structures. The possibility of theoretical parameter uncertainties as well as measurement errors contributing to this result have been considered. It is recommended that the spectrometers aboard SOHO acquire as many diagnostic ratios as possible for purposes of cross-checking, and to ensure that over-reliance upon potentially “inappropriate” ratios does not occur. Intensity ratios of emission lines from different stages of ionization of iron were used to calculate temperatures. Because Fe XVII emission is present in the active region spectra but absent in the quiet Sun spectra, the maximum derived active region temperatures exceed the quiet Sun values by factors ~ 1.7 . Consistent temperatures are derived for all of the features observed from ratios which include only Fe X through Fe XIII. When Fe XIV through Fe XVI are included, the active region temperatures are statistically significantly greater (by factors ~ 1.2) than their

quiet Sun counterparts. Differential emission measure distributions were determined for the active region and quiet Sun spectra. All of the DEM curves show extrema between $\log T = 6.1$ and 6.2 , but only the active region DEM curves show a second extremum between $\log T \sim 6.7$ and 6.8 . The high-temperature DEM peak exceeds the low-temperature DEM peak for the 1991 active region, but not for the 1993 active region. This is consistent with the fact that a higher maximum temperature is derived from line intensity ratios for the 1991 than for the 1993 active region, and may be a manifestation of the enhanced activity in the 1991 active region as surmised from its greater measured photospheric magnetic fields.

Acknowledgments: JWB acknowledges NASA support through contract NASW-4933. We acknowledge valuable discussions with J.L.R. Saba, M. Landini, H.E. Mason, and P.R. Young.

TABLE 1
SERTS 1993 Active Region Characteristic Spectrum

No.	Ion	Lambda (Å)	Intensity (erg/cm ² /s/sr)	Sigma (same)	Width (mÅ)	Sigma (mÅ)
---	---	-----	-----	-----	-----	-----
1	Si XI	303.317	2.84e+03	3.21e+02	8.10e+01	4.17e+00
2	He II	303.782	3.34e+04	3.77e+03	7.62e+01	3.91e+00
3	Mn XIV	304.860	1.53e+02	2.45e+01	8.94e+01	8.96e+00
	+Fe XV					
4	Fe XI	308.543	3.37e+01	1.32e+01	5.61e+01	1.62e+01
5	Mg VIII	311.783	5.25e+01	1.09e+01	5.50e+01	7.78e+00
	+Ni IV					
6	Fe XIII	312.171	1.42e+02	2.22e+01	6.86e+01	6.61e+00
7	Fe XV	312.569	5.72e+01	1.43e+01	6.35e+01	1.12e+01
	+Co XVII					
8	---	312.874	5.17e+01	1.30e+01	6.33e+01	1.12e+01
9	Mg VIII	313.744	9.94e+01	1.52e+01	6.87e+01	6.40e+00
10	Si VIII	314.358	8.48e+01	1.60e+01	6.75e+01	8.47e+00
11	Mg VIII	315.029	3.64e+02	4.25e+01	7.96e+01	4.48e+00
12	Si VIII	316.223	1.89e+02	2.92e+01	8.72e+01	8.27e+00
13	Mg VIII	317.018	9.95e+01	2.07e+01	8.96e+01	1.27e+01
14	Fe XIII	318.121	1.63e+02	2.35e+01	7.53e+01	6.42e+00
15	Mg VII	319.033	1.04e+02	1.64e+01	8.91e+01	8.69e+00
	+Ni XV					
16	Si VIII	319.852	3.16e+02	3.91e+01	7.79e+01	4.97e+00
17	Ni XVIII	320.568	1.06e+02	1.57e+01	7.63e+01	6.74e+00
18	Fe XIII	320.809	3.96e+02	4.64e+01	6.98e+01	3.94e+00
19	---	321.035	3.72e+01	1.14e+01	4.90e+01	1.08e+01
20	Fe XIII	321.479	7.79e+01	1.44e+01	6.29e+01	7.71e+00
21	Fe XV	321.809	4.22e+01	1.13e+01	5.51e+01	1.05e+01
22	Fe XV	327.045	2.14e+02	2.72e+01	7.76e+01	5.28e+00
23	Cr XIII	328.270	2.48e+02	3.12e+01	8.18e+01	5.43e+00
24	Al I	332.799	4.91e+02	5.82e+01	9.37e+01	5.47e+00
25	Fe XIV	334.191	2.95e+03	3.33e+02	7.33e+01	3.77e+00
26	Fe XVI	335.418	1.84e+04	2.11e+03	7.12e+01	3.80e+00
27	Fe XII	338.290	4.03e+02	4.98e+01	7.86e+01	5.02e+00
28	Mg VIII	339.014	2.77e+02	3.63e+01	1.04e+02	7.46e+00
29	Fe XI	341.136	2.99e+02	3.98e+01	8.34e+01	6.17e+00
30	Si IX	341.987	1.84e+02	2.68e+01	7.24e+01	6.26e+00
31	---	343.664	7.59e+01	2.87e+01	6.99e+01	1.95e+01
32	Si IX	345.148	5.02e+02	6.61e+01	8.70e+01	6.32e+00
33	Fe X	345.753	4.30e+02	5.13e+01	7.37e+01	4.35e+00
34	Fe XII	346.867	4.69e+02	5.67e+01	8.58e+01	5.24e+00
35	Si X	347.421	1.17e+03	1.33e+02	8.72e+01	4.58e+00
36	Fe XIII	348.199	8.65e+02	1.00e+02	7.52e+01	4.14e+00
37	Fe XI	349.129	3.20e+02	5.55e+01	1.80e+02	2.09e+01
	+Mg VI					
38	Si IX	349.895	8.36e+02	9.90e+01	9.45e+01	5.49e+00
39	Fe XVII	350.521	7.20e+01	2.57e+01	7.92e+01	2.09e+01
40	Fe XII	352.131	8.14e+02	9.43e+01	7.39e+01	4.07e+00
41	Fe II	352.699	7.66e+02	8.74e+01	7.89e+01	4.18e+00
42	Fe XIV	353.856	1.30e+03	1.47e+02	7.91e+01	4.10e+00
43	Si I	356.052	1.19e+03	1.40e+02	9.41e+01	5.30e+00
44	Fe II	358.694	2.83e+02	5.08e+01	1.13e+02	1.33e+01
45	Ne V	359.384	1.14e+02	2.22e+01	7.60e+01	9.89e+00
46	Fe XIII	359.665	8.03e+02	9.74e+01	7.49e+01	4.59e+00
47	Fe XIII	359.851	1.91e+02	2.75e+01	7.35e+01	6.27e+00
48	Fe XVI	360.782	9.31e+03	1.06e+03	7.57e+01	3.96e+00
49	Mn IV	361.006	1.26e+02	2.34e+01	6.11e+01	7.51e+00
50	Fe XII	364.494	9.88e+02	1.14e+02	8.59e+01	4.66e+00
51	Mg VII	367.698	1.67e+02	3.66e+01	8.91e+01	1.39e+01
52	Mg IX	368.093	3.13e+03	3.64e+02	1.15e+02	6.35e+00
53	Fe II	369.204	1.90e+02	4.06e+01	1.15e+02	1.68e+01
54	Mn IVb	384.768	1.10e+02	3.23e+01	8.64e+01	1.83e+01
55	Cr XIV	389.903	1.64e+02	3.57e+01	7.31e+01	1.10e+01
56	Ne VI	401.996	1.54e+02	3.14e+01	1.06e+02	1.47e+01
57	Fe XV	417.296	7.71e+02	9.40e+01	8.82e+01	5.47e+00
58	S XIV	417.688	2.15e+02	4.05e+01	9.11e+01	1.14e+01

TABLE 2
SERTS 1993 Quiet Sun Characteristic Spectrum

No.	Ion	Lambda (Å)	Intensity (erg/cm2/s/sr)	Sigma (same)	Width (mÅ)	Sigma (mÅ)
---	---	---	---	---	---	---
1	Si II	303.319	4.51e+02	5.09e+01	8.85e+01	4.55e+00
2	He II	303.782	6.94e+03	7.78e+02	9.20e+01	4.63e+00
3	Mn XIV	304.890	1.46e+01	4.23e+00	8.71e+01	1.80e+01
	+Fe IV					
4	Fe XIII	311.574	7.51e+00	1.90e+00	7.37e+01	1.32e+01
5	Mg VIII	311.783	1.75e+01	3.97e+00	6.58e+01	1.04e+01
	+Ni IV					
6	Fe XIII	312.171	2.41e+01	4.12e+00	6.22e+01	6.81e+00
7	---	312.904	9.31e+00	3.04e+00	7.54e+01	1.82e+01
8	Mg VIII	313.732	1.84e+01	3.03e+00	5.67e+01	5.89e+00
9	Si VIII	314.353	2.70e+01	3.96e+00	8.66e+01	7.58e+00
10	Mg VIII	315.022	6.88e+01	8.17e+00	9.10e+01	5.32e+00
11	Si VIII	316.219	4.29e+01	6.27e+00	9.12e+01	7.93e+00
12	Mg VIII	317.026	2.26e+01	3.31e+00	1.14e+02	9.98e+00
13	---	317.255	2.04e+01	4.90e+00	1.27e+02	2.14e+01
14	Fe XIII	318.129	1.16e+01	2.82e+00	6.53e+01	1.12e+01
15	Si VIII	319.843	7.53e+01	9.12e+00	8.19e+01	5.01e+00
16	Fe XIII	320.802	5.73e+01	6.75e+00	9.02e+01	5.18e+00
17	---	320.996	1.06e+01	1.57e+00	5.21e+01	4.60e+00
18	Fe XIII	321.464	2.16e+01	3.62e+00	8.89e+01	9.49e+00
19	---	326.361	1.69e+01	3.00e+00	8.33e+01	9.64e+00
20	Fe IV	327.041	2.10e+01	4.26e+00	1.01e+02	1.39e+01
21	Cr XIII	328.270	5.27e+01	6.40e+00	9.40e+01	5.77e+00
22	---	330.785	8.30e+00	2.22e+00	5.18e+01	9.87e+00
23	Al I	332.800	1.20e+02	1.39e+01	9.63e+01	5.32e+00
24	Fe XIV	334.187	3.62e+02	4.09e+01	8.12e+01	4.21e+00
25	Fe XVI	335.417	7.35e+02	8.32e+01	8.37e+01	4.33e+00
26	Fe XII	338.289	5.91e+01	7.90e+00	7.94e+01	5.92e+00
27	Mg VIII	339.017	2.98e+01	5.15e+00	8.62e+01	9.62e+00
28	Fe XI	341.141	5.65e+01	7.28e+00	7.35e+01	5.12e+00
29	Si IX	341.982	5.85e+01	1.00e+01	8.66e+01	9.53e+00
30	Si IX	344.974	2.97e+01	3.75e+00	5.96e+01	3.96e+00
31	Si IX	345.143	1.23e+02	1.77e+01	8.52e+01	7.24e+00
32	Fe X	345.748	1.03e+02	1.25e+01	7.68e+01	4.67e+00
33	Fe XII	346.871	9.06e+01	1.08e+01	7.42e+01	4.35e+00
34	Si I	347.419	3.31e+02	3.72e+01	8.77e+01	4.46e+00
35	Fe XIII	348.196	2.27e+02	2.57e+01	8.23e+01	4.29e+00
36	Fe XI	349.112	8.17e+01	1.55e+01	1.70e+02	2.17e+01
	+Mg VI					
37	Si IX	349.885	1.98e+02	2.29e+01	9.72e+01	5.30e+00
38	Fe XII	352.127	1.96e+02	2.24e+01	7.42e+01	3.94e+00
39	Fe XI	352.694	2.08e+02	2.48e+01	8.40e+01	4.94e+00
40	Fe XIV	353.851	1.18e+02	1.41e+01	8.15e+01	4.82e+00
41	Si I	356.054	2.52e+02	2.95e+01	9.63e+01	5.40e+00
42	Fe XI	358.661	5.09e+01	8.83e+00	9.90e+01	1.11e+01
43	Ne V	359.388	2.89e+01	7.15e+00	5.74e+01	9.99e+00
44	Fe XIII	359.658	1.34e+02	1.76e+01	8.89e+01	6.40e+00
45	Fe XIII	359.853	5.64e+01	7.23e+00	1.01e+02	7.09e+00
46	Fe XVI	360.785	3.52e+02	4.04e+01	1.02e+02	5.46e+00
47	---	361.746	2.42e+01	7.88e+00	5.12e+01	1.21e+01
48	Fe XII	364.490	2.31e+02	2.68e+01	8.83e+01	4.87e+00
49	Fe I	365.570	3.12e+01	6.02e+00	1.13e+02	1.45e+01
50	Mg IX	368.085	6.03e+02	6.95e+01	1.03e+02	5.60e+00
51	Fe XI	369.159	4.12e+01	9.75e+00	1.21e+02	2.03e+01
52	Ne VI	401.957	3.69e+01	9.24e+00	1.28e+02	2.26e+01
53	---	405.374	1.86e+01	4.75e+00	5.23e+01	9.46e+00
54	---	407.170	3.08e+01	6.50e+00	7.95e+01	1.15e+01
55	Ne V	416.224	1.52e+01	3.85e+00	6.07e+01	1.09e+01
56	Fe XV	417.294	4.15e+01	6.38e+00	7.42e+01	6.98e+00

TABLE 3
SERTS 1991 Active Region Characteristic Spectrum

No.	Ion	Lambda (Å)	Intensity (erg/cm ² /s/sr)	Sigma (same)	Width (mÅ)	Sigma (mÅ)
1	Si XII	303.323	9.24e+02	1.04e+02	8.95e+01	4.54e+00
2	He II	303.782	1.71e+04	1.92e+03	9.02e+01	4.62e+00
3	Mn XIV	304.869	8.42e+01	1.37e+01	8.44e+01	8.59e+00
	+Fe XV					
4	Fe XIII	312.174	5.00e+01	1.00e+01	8.27e+01	1.12e+01
5	Fe IV	312.558	5.05e+01	9.60e+00	7.12e+01	9.02e+00
	+Co XVII					
6	Mg VIII	313.759	3.42e+01	8.06e+00	4.88e+01	8.05e+00
7	Mg VIII	315.029	1.25e+02	1.64e+01	7.42e+01	5.35e+00
8	Si VIIIb	316.196	7.19e+01	1.48e+01	1.48e+02	2.08e+01
9	Mg VIII	317.026	4.64e+01	8.74e+00	8.35e+01	1.05e+01
10	Fe XIII	318.126	5.29e+01	7.94e+00	7.35e+01	6.67e+00
11	Mg VII	319.037	5.84e+01	1.21e+01	1.14e+02	1.61e+01
	+Ni XV					
12	Si VIII	319.842	7.08e+01	1.02e+01	5.71e+01	4.85e+00
13	Ni XVIII	320.567	2.20e+02	2.69e+01	7.65e+01	4.80e+00
14	Fe XIII	320.806	1.29e+02	1.80e+01	7.05e+01	5.67e+00
15	Fe XIII	321.477	2.37e+01	6.64e+00	4.11e+01	8.23e+00
16	Fe IV	327.043	1.44e+02	1.85e+01	7.59e+01	5.22e+00
17	Cr XIII	328.271	1.18e+02	1.70e+01	8.24e+01	7.00e+00
18	Al X	332.797	1.96e+02	2.42e+01	8.71e+01	5.60e+00
19	Fe XIV	334.188	9.97e+02	1.12e+02	7.50e+01	3.82e+00
20	Fe XVI	335.413	1.52e+04	1.71e+03	8.56e+01	4.39e+00
21	Fe XII	338.287	1.42e+02	1.95e+01	9.84e+01	7.74e+00
22	Mg VIII	338.996	6.67e+01	1.30e+01	8.35e+01	1.09e+01
23	Fe XI	341.127	8.38e+01	1.45e+01	7.94e+01	8.83e+00
24	Si IX	341.975	5.52e+01	1.99e+01	9.30e+01	2.51e+01
25	Si IX	344.990	4.56e+01	1.49e+01	9.20e+01	2.22e+01
26	Si IX	345.132	1.14e+02	2.23e+01	8.24e+01	1.08e+01
27	Fe X	345.733	1.12e+02	1.64e+01	7.49e+01	6.49e+00
28	Fe XII	346.867	1.51e+02	2.40e+01	7.82e+01	7.71e+00
29	Si X	347.411	3.12e+02	3.87e+01	8.51e+01	5.47e+00
30	Fe XIII	348.190	2.49e+02	3.33e+01	7.67e+01	5.70e+00
31	Fe XI	349.137	1.58e+02	2.96e+01	1.50e+02	1.87e+01
	+Mg VI					
32	Si IX	349.887	1.91e+02	2.56e+01	7.39e+01	5.57e+00
33	Fe XVII	350.467	1.30e+02	2.79e+01	8.78e+01	1.30e+01
34	Fe XII	352.116	2.44e+02	3.35e+01	8.19e+01	6.43e+00
35	Fe XI	352.685	1.59e+02	2.43e+01	5.68e+01	5.29e+00
36	Fe XIV	353.846	5.90e+02	6.89e+01	8.70e+01	4.87e+00
37	Si X	356.040	2.52e+02	3.42e+01	7.97e+01	6.09e+00
38	Fe XI	358.678	9.29e+01	2.21e+01	8.35e+01	1.39e+01
39	He V	359.388	6.39e+01	1.44e+01	6.16e+01	9.59e+00
40	Fe XIII	359.655	1.78e+02	3.22e+01	9.50e+01	1.12e+01
41	Fe XIII	359.856	3.33e+01	1.78e+01	3.69e+01	1.47e+01
42	Fe XVI	360.768	7.77e+03	8.73e+02	8.39e+01	4.25e+00
43	Fe XII	364.477	2.43e+02	3.41e+01	8.28e+01	6.72e+00
44	Fe X	365.574	4.16e+01	1.13e+01	7.66e+01	1.53e+01
45	Mg IX	368.080	8.60e+02	1.05e+02	1.13e+02	7.03e+00
46	Fe XI	369.182	7.33e+01	1.83e+01	6.92e+01	1.22e+01
47	Cr XIV	389.875	1.04e+02	2.10e+01	7.66e+01	1.05e+01
48	He VI	401.958	1.29e+02	2.23e+01	1.05e+02	1.17e+01
49	He VI	403.282	8.84e+01	1.74e+01	1.24e+02	1.74e+01
	+Mg VI					
50	He V	416.222	6.38e+01	1.31e+01	9.15e+01	1.28e+01
51	Fe IV	417.272	3.49e+02	4.28e+01	9.47e+01	5.93e+00
52	S XIV	417.657	2.12e+02	2.99e+01	1.10e+02	9.01e+00

TABLE 4
SERTS 1991 Quiet Sun Characteristic Spectrum
(Frame 1)

No.	Ion	Lambda (Å)	Intensity (erg/cm2/s/sr)	Sigma (same)	Width (mÅ)	Sigma (mÅ)
---	---	---	---	---	---	---
1	Si XII	303.323	8.93e+02	1.01e+02	9.15e+01	4.73e+00
2	He II	303.782	7.76e+03	8.69e+02	1.11e+02	5.57e+00
3	Al IX	305.062	3.97e+01	1.00e+01	3.80e+01	6.76e+00
4	Fe XIII	311.561	1.29e+01	5.19e+00	5.43e+01	1.61e+01
5	Fe XIII	312.181	4.20e+01	8.75e+00	4.06e+01	5.78e+00
6	Mg VIII	313.741	7.30e+01	1.25e+01	6.55e+01	7.20e+00
7	Si VIII	314.362	4.70e+01	1.44e+01	7.86e+01	1.75e+01
8	Mg VIII	315.025	1.79e+02	2.28e+01	8.17e+01	5.61e+00
9	Si VIII	316.228	1.07e+02	1.64e+01	6.45e+01	6.05e+00
10	Mg VIII	317.016	3.54e+01	9.85e+00	5.93e+01	1.18e+01
11	Fe XIII	318.126	5.67e+01	1.24e+01	5.73e+01	8.61e+00
12	Si VIII	319.850	2.17e+02	2.79e+01	8.35e+01	5.77e+00
13	Fe XIII	320.811	8.39e+01	1.57e+01	8.05e+01	9.96e+00
14	---	320.986	3.18e+01	6.62e+00	1.02e+02	1.49e+01
15	Fe XIII	321.449	2.32e+01	9.91e+00	3.78e+01	1.19e+01
16	---	326.386	3.63e+01	9.67e+00	4.27e+01	8.10e+00
17	Cr XIII	328.262	7.02e+01	1.56e+01	1.13e+02	1.73e+01
18	Al X	332.804	2.57e+02	3.84e+01	9.20e+01	8.28e+00
19	Fe XIV	334.191	6.06e+02	6.94e+01	8.16e+01	4.36e+00
20	Fe XVI	335.422	1.42e+03	1.64e+02	8.80e+01	4.81e+00
21	Fe XII	338.295	2.14e+02	3.12e+01	8.59e+01	7.45e+00
22	Mg VIII	339.019	7.58e+01	1.98e+01	4.74e+01	8.78e+00
23	Fe XI	341.155	2.50e+02	4.03e+01	9.74e+01	9.85e+00
24	Si IX	341.965	1.81e+02	3.15e+01	8.04e+01	9.05e+00
25	Si IX	344.971	7.89e+01	2.20e+01	4.81e+01	9.59e+00
26	Si IX	345.135	3.30e+02	5.41e+01	8.23e+01	8.51e+00
27	Fe X	345.740	2.72e+02	4.41e+01	6.95e+01	7.07e+00
28	Fe XII	346.853	2.55e+02	4.15e+01	6.49e+01	6.64e+00
29	Si X	347.409	8.91e+02	1.08e+02	8.81e+01	5.43e+00
30	Fe XIII	348.187	5.36e+02	7.00e+01	8.50e+01	6.07e+00
31	Fe XI	349.109	2.37e+02	4.26e+01	1.46e+02	1.72e+01
+Mg VI						
32	Si IX	349.876	5.16e+02	6.18e+01	8.21e+01	4.90e+00
33	Fe XII	352.121	4.65e+02	6.15e+01	8.25e+01	6.03e+00
34	Fe XI	352.682	4.91e+02	6.64e+01	8.01e+01	6.10e+00
35	Fe XIV	353.847	1.59e+02	3.91e+01	6.68e+01	1.15e+01
36	---	355.671	6.72e+01	2.89e+01	3.88e+01	1.24e+01
37	Si X	356.043	5.57e+02	7.18e+01	9.35e+01	6.51e+00
38	Fe XIII	359.651	1.89e+02	4.30e+01	8.69e+01	1.38e+01
39	Fe XIII	359.862	1.10e+02	4.02e+01	9.02e+01	2.44e+01
40	Fe XVI	360.788	6.31e+02	8.61e+01	9.52e+01	7.37e+00
41	Fe XII	364.485	4.35e+02	5.87e+01	8.02e+01	6.08e+00
42	Mg IX	368.079	1.41e+03	1.63e+02	1.02e+02	5.51e+00
43	Fe XI	369.189	1.39e+02	3.97e+01	8.82e+01	1.74e+01
44	Ne VI	401.959	3.42e+01	1.25e+01	3.81e+01	1.02e+01
45	Fe IV	417.279	6.57e+01	2.19e+01	2.86e+01	6.91e+00
46	S XIV	417.680	6.43e+01	2.39e+01	3.92e+01	1.07e+01

TABLE 5
SERTS 1991 Off-Limb Characteristic Spectrum

No.	Ion	Lambda (Å)	Intensity (erg/cm ² /s/sr)	Sigma (same)	Width (mÅ)	Sigma (mÅ)
---	---	---	---	---	---	---
1	Si XII	303.327	1.99e+03	2.23e+02	9.11e+01	4.60e+00
2	He II	303.782	2.14e+03	2.43e+02	1.24e+02	6.47e+00
3	Mn XIV	304.861	6.61e+01	1.68e+01	5.54e+01	9.93e+00
	+Fe IV					
4	Al IX	305.094	4.70e+01	1.89e+01	7.10e+01	2.09e+01
5	Fe XI	308.556	5.09e+01	1.31e+01	5.35e+01	9.78e+00
6	Fe XIIIb	311.543	3.71e+01	1.46e+01	4.76e+01	1.41e+01
7	Fe XIII	312.177	1.18e+02	2.07e+01	5.06e+01	5.72e+00
8	---	312.892	7.85e+01	1.93e+01	8.93e+01	1.55e+01
9	Mg VIII	313.746	1.06e+02	1.68e+01	6.82e+01	6.73e+00
10	Si VIII	314.347	8.49e+01	1.92e+01	7.51e+01	1.17e+01
11	Mg VIII	315.024	1.38e+02	2.40e+01	6.92e+01	7.78e+00
12	Si VIII	316.218	1.43e+02	2.67e+01	9.15e+01	1.13e+01
13	Mg VIII	317.026	6.23e+01	1.60e+01	6.69e+01	1.21e+01
14	Fe XIII	318.128	8.77e+01	1.46e+01	7.88e+01	8.37e+00
15	Mg VII	319.040	2.06e+01	1.04e+01	4.37e+01	1.65e+01
	+Si IV					
16	Si VIII	319.856	2.35e+02	3.11e+01	7.34e+01	5.38e+00
17	Fe XIII	320.812	2.45e+02	3.15e+01	6.82e+01	4.73e+00
18	Fe XIII	321.477	1.12e+02	2.46e+01	6.95e+01	1.06e+01
19	---	326.364	5.98e+01	1.59e+01	4.73e+01	8.94e+00
20	Fe IV	327.047	7.24e+01	2.21e+01	5.23e+01	1.16e+01
21	Cr XIII	328.283	2.03e+02	3.34e+01	5.88e+01	6.14e+00
22	---	331.941	1.25e+02	2.74e+01	8.12e+01	1.22e+01
23	Al X	332.804	5.20e+02	6.39e+01	8.34e+01	5.27e+00
24	Fe XIV	334.192	2.18e+03	2.47e+02	7.87e+01	4.09e+00
25	Fe XVI	335.422	7.28e+03	8.20e+02	8.49e+01	4.34e+00
26	Fe XII	338.289	4.88e+02	7.23e+01	1.02e+02	9.06e+00
27	Fe XI	341.129	4.27e+02	6.39e+01	1.07e+02	9.68e+00
28	Si IX	341.965	4.27e+02	6.83e+01	1.19e+02	1.19e+01
29	Si IX	344.967	1.46e+02	2.34e+01	3.72e+01	3.70e+00
30	Si IX	345.141	5.63e+02	8.26e+01	7.18e+01	6.28e+00
31	Fe X	345.745	4.80e+02	7.02e+01	7.01e+01	6.10e+00
32	Fe XII	346.866	7.34e+02	1.02e+02	7.74e+01	6.23e+00
33	Si X	347.415	1.61e+03	1.93e+02	8.52e+01	5.04e+00
34	Fe XIII	348.189	1.35e+03	1.56e+02	8.03e+01	4.42e+00
35	Si IX	349.885	8.50e+02	1.27e+02	1.00e+02	8.99e+00
36	Fe XVII	350.505	1.10e+02	3.22e+01	5.29e+01	1.12e+01
37	Fe XII	352.126	1.15e+03	1.37e+02	7.87e+01	4.61e+00
38	Fe XI	352.690	1.05e+03	1.26e+02	8.70e+01	5.28e+00
39	Fe XIV	353.845	7.96e+02	1.08e+02	7.99e+01	6.09e+00
40	Si X	356.050	1.08e+03	1.35e+02	8.55e+01	5.66e+00
41	Fe XVIIb	358.267	3.73e+02	9.49e+01	1.56e+02	2.83e+01
42	Fe XIII	359.661	5.46e+02	9.75e+01	5.89e+01	6.87e+00
43	Fe XIII	359.840	1.62e+02	5.81e+01	6.87e+01	1.88e+01
44	Fe XVI	360.776	3.27e+03	3.76e+02	9.32e+01	5.04e+00
45	Mn IV	360.957	1.40e+02	3.13e+01	5.26e+01	8.17e+00
46	Fe XII	364.485	1.20e+03	1.43e+02	8.47e+01	5.00e+00
47	Mg IX	368.083	1.98e+03	2.65e+02	1.20e+02	8.96e+00
48	---	369.056	1.86e+02	4.36e+01	5.05e+01	8.27e+00
49	Fe XI	369.181	1.84e+02	8.05e+01	4.80e+01	1.56e+01
50	Cr XIV	389.915	2.19e+02	5.82e+01	7.70e+01	1.46e+01
51	Fe XV	417.279	4.78e+02	9.59e+01	1.05e+02	1.42e+01

TABLE 6

Density- and Temperature-Insensitive Line Ratios

<u>Line Ratio</u>	<u>Theoretical</u>	<u>1993 AR</u>	<u>1993 QS</u>	<u>1991 AR</u>	<u>1991 QS</u>	<u>1991 L</u>	<u>1989 AR</u>
Fe XVI 360.8/335.4	0.482	0.506±0.082	0.479±0.077	0.511±0.081	0.444±0.079	0.449±0.072	0.415±0.094
Fe XV 327.0/417.3	0.314±0.047	0.278±0.049	0.506±0.129	0.413±0.073	—	0.151±0.055	0.258±0.047
Fe XIII 359.8/348.2	0.293	0.221±0.041	0.248±0.042	0.134±0.074	0.205±0.080	0.120±0.045	0.175±0.040
Fe XIII 320.8/311.6	6.63	—	7.63±2.13	—	6.50±2.89	6.60±2.73	4.22±1.25
Fe XIII 321.5/312.2	0.504	0.549±0.133	0.896±0.215	0.474±0.163	0.552±0.263	0.949±0.267	0.383±0.102
Fe XII 346.9/364.5	0.341±0.029	0.475±0.079	0.392±0.065	0.621±0.132	0.586±0.124	0.612±0.112	0.287±0.049
Fe XII 352.1/364.5	0.672±0.028	0.824±0.135	0.848±0.138	1.00±0.20	1.07±0.20	0.958±0.161	0.618±0.100
Fe XI 369.2/352.7	0.303	0.248±0.060	0.198±0.052	0.461±0.135	0.283±0.089	0.175±0.079	0.292±0.053
Fe XI 341.1/369.2	0.935±0.195	1.57±0.40	1.37±0.37	1.14±0.35	1.80±0.59	2.32±1.07	0.984±0.202
Fe XI 341.1/358.7	1.57	1.06±0.24	1.11±0.24	0.902±0.265	—	—	0.514±0.103
Fe X 365.6/345.7	0.427	—	0.303±0.069	0.371±0.115	—	—	0.567±0.107
Si IX 342.0/349.9	0.326±0.051	0.220±0.041	0.295±0.061	0.289±0.111	0.351±0.074	0.502±0.110	0.210±0.043
Si IX 345.0/345.1	0.257±0.010	—	0.241±0.046	0.400±0.152	0.239±0.077	0.259±0.056	0.244±0.068
Si IX 349.9/345.1	1.42±0.19	1.67±0.29	1.61±0.30	1.68±0.40	1.56±0.32	1.51±0.32	0.970±0.360
Si VIII 314.3/319.8	0.354±0.007	0.268±0.061	0.359±0.068	—	0.217±0.072	0.361±0.095	0.479±0.108
Si VIII 319.8/316.2	1.49±0.02	1.67±0.33	1.76±0.33	>0.985	2.03±0.41	1.64±0.38	1.27±0.24

TABLE 7

Densities Derived from Line Intensity Ratios

<u>Line Ratio</u>	<u>1993 AR</u>	<u>1993 QS</u>	<u>1991 AR</u>	<u>1991 QS</u>	<u>1991 L</u>	<u>1989 AR</u>
Fe XV 321.8/327.0	9.27 ± 0.24	--	--	--	--	10.16 ± 0.48
Fe XIV 353.8/334.2	9.68 ± 0.12	9.44 ± 0.12	9.99 ± 0.19	9.29 ± 0.16	9.52 ± 0.14	9.71 ± 0.15
Fe XIII 320.8/348.2	8.97 ± 0.14	8.51 ± 0.10	9.07 ± 0.17	8.27 ± 0.10	8.33 ± 0.08	9.65 ± 0.08
Fe XIII 359.7/348.2	9.52 ± 0.10	9.18 ± 0.15	9.34 ± 0.18	8.71 ± 0.22	8.84 ± 0.19	9.63 ± 0.09
Fe XIII 320.8/359.7	7.64 ± 0.26	7.43 ± 0.25	8.22 ± 0.39	7.48 ± 0.42	7.50 ± 0.32	≥ 8.93
Fe XIII 359.8/359.7	9.85 ± 0.12	9.40 ± 0.18	≥ 9.71	9.05 ± 0.50	9.70 ± 0.30	≥ 10.0
Fe XIII 320.8/359.8	9.21 ± 0.15	8.62 ± 0.12	9.59 ± 0.39	8.44 ± 0.23	8.94 ± 0.32	≥ 9.81
Fe XIII 318.1/320.8	7.88, 9.89	8.86, 9.12	7.89, 9.88	7.20, 10.56	8.10, 9.71	7.42, 10.30
Fe XII 338.3/352.1	10.20 ± 0.27	9.38 ± 0.23	10.43 ± 0.26	10.06 ± 0.26	9.94 ± 0.33	10.31 ± 0.26

TABLE 8

Polynomial Fitting Parameters for Deriving Temperatures from Line Intensity Ratios in a 10^9 cm^{-3} Plasma

Iron Ion Ratio			a0	a1	a2	a3
-----			-----	-----	-----	-----
XVII	350.5/XVI	335.4	8.000	9.54e-01	1.93e-01	1.53e-02
XVII	350.5/XV	417.3	6.681	1.77e-01	2.09e-02	1.46e-03
XVI	335.4/XV	417.3	6.124	1.48e-01	3.94e-02	4.72e-03
XVI	335.4/XIV	334.2	6.236	1.09e-01	7.83e-03	1.97e-03
XVI	335.4/XIII	348.2	6.233	7.59e-02	4.11e-03	4.66e-04
XVI	335.4/XII	352.1	6.209	5.87e-02	1.70e-03	3.20e-04
XV	417.3/XIV	334.2	6.396	2.90e-01	7.07e-02	1.83e-02
XV	417.3/XIII	348.2	6.311	1.34e-01	1.32e-02	1.45e-03
XV	417.3/XII	352.1	6.251	8.60e-02	5.35e-03	5.92e-04
XIV	334.2/XIII	348.2	6.227	2.51e-01	4.59e-02	6.89e-03
XIV	334.2/XII	352.1	6.177	1.24e-01	1.11e-02	1.38e-03
XIII	348.2/XII	352.1	6.123	2.52e-01	4.50e-02	8.56e-03
XIII	348.2/XI	341.1	6.057	1.19e-01	1.02e-02	1.09e-03
XIII	348.2/X	345.7	6.083	8.52e-02	5.26e-03	3.36e-04
XII	352.1/XI	341.1	5.993	2.25e-01	3.65e-02	8.80e-03
XII	352.1/X	345.7	6.062	1.28e-01	1.20e-02	1.51e-03
XI	341.1/X	345.7	6.144	3.02e-01	6.23e-02	8.34e-03

TABLE 9

Polynomial Fitting Paramaters for Deriving Temperatures from Line Intensity Ratios in a 10^{10}
 cm^{-3} Plasma

Iron Ion Ratio		a0	a1	a2	a3
-----		-----	-----	-----	-----
XVII 350.5/XVI	335.4	8.001	9.55e-01	1.93e-01	1.53e-02
XVII 350.5/XV	417.3	6.677	1.76e-01	2.10e-02	1.48e-03
XVI 335.4/XV	417.3	6.119	1.46e-01	3.90e-02	4.96e-03
XVI 335.4/XIV	334.2	6.218	1.07e-01	6.67e-03	2.07e-03
XVI 335.4/XIII	348.2	6.202	7.25e-02	3.57e-03	4.50e-04
XVI 335.4/XII	352.1	6.203	5.87e-02	1.57e-03	3.35e-04
XV 417.3/XIV	334.2	6.357	2.72e-01	6.43e-02	1.90e-02
XV 417.3/XIII	348.2	6.261	1.23e-01	1.13e-02	1.43e-03
XV 417.3/XII	352.1	6.245	8.56e-02	5.27e-03	6.21e-04
XIV 334.2/XIII	348.2	6.166	2.29e-01	3.92e-02	5.82e-03
XIV 334.2/XII	352.1	6.185	1.27e-01	1.16e-02	1.42e-03
XIII 348.2/XII	352.1	6.208	2.90e-01	5.83e-02	1.00e-02
XIII 348.2/XI	341.1	6.108	1.27e-01	1.16e-02	1.13e-03
XIII 348.2/X	345.7	6.120	8.99e-02	5.74e-03	3.48e-04
XII 352.1/XI	341.1	6.016	2.29e-01	3.70e-02	7.95e-03
XII 352.1/X	345.7	6.077	1.30e-01	1.22e-02	1.45e-03
XI 341.1/X	345.7	6.150	3.06e-01	6.31e-02	8.34e-03

TABLE 10

Temperature Logarithms from Line Intensity Ratios Among Various Iron Ionization Stages

<u>Line Ratio</u>	<u>1993 AR</u>	<u>1993 QS</u>	<u>1991 AR</u>	<u>1991 QS</u>	<u>1991 L</u>	<u>1989 AR</u>
XVII 350.5/XVI 335.4	6.61±0.05	—	6.72±0.04	—	6.81±0.06	6.53±0.03
XVII 350.5/XV 417.3	6.52±0.02	—	6.61±0.02	—	6.57±0.02	6.49±0.02
XVI 335.4/XV 417.3	6.41±0.02	6.38±0.02	6.49±0.02	6.40±0.04	6.36±0.03	6.44±0.03
XVI 335.4/XIV 334.2	6.32±0.01	6.26±0.01	6.37±0.01	6.27±0.01	6.29±0.01	6.37±0.02
XVI 335.4/XIII 348.2	6.32±0.02	6.26±0.02	6.36±0.02	6.25±0.02	6.27±0.02	6.38±0.02
XVI 335.4/XII 352.1	6.29±0.01	6.24±0.01	6.32±0.01	6.24±0.01	6.25±0.01	6.32±0.01
XV 417.3/XIV 334.2	6.23±0.02	6.16±0.02	6.26±0.02	6.15±0.04	6.22±0.03	6.30±0.02
XV 417.3/XIII 348.2	6.28±0.03	6.20±0.02	6.30±0.03	6.18±0.03	6.23±0.03	6.34±0.03
XV 417.3/XII 352.1	6.25±0.01	6.19±0.01	6.26±0.01	6.18±0.01	6.22±0.01	6.28±0.01
XIV 334.2/XIII 348.2	6.34±0.04	6.25±0.04	6.36±0.05	6.21±0.04	6.25±0.04	6.39±0.05
XIV 334.2/XII 352.1	6.26±0.01	6.22±0.01	6.26±0.01	6.20±0.01	6.22±0.01	6.27±0.01
XIII 348.2/XII 352.1	6.17±0.05	6.18±0.05	6.17±0.05	6.18±0.05	6.18±0.05	6.15±0.05
XIII 348.2/XI 341.1	6.14±0.03	6.16±0.03	6.14±0.03	6.12±0.03	6.15±0.03	6.15±0.03
XIII 348.2/X 345.7	6.13±0.02	6.13±0.02	6.13±0.02	6.13±0.02	6.14±0.02	6.12±0.02
XII 352.1/XI 341.1	6.11±0.02	6.14±0.02	6.12±0.03	6.07±0.03	6.11±0.03	6.15±0.03
XII 352.1/X 345.7	6.11±0.01	6.11±0.01	6.11±0.01	6.10±0.02	6.12±0.01	6.11±0.01
XI 341.1/X 345.7	6.10±0.02	6.07±0.02	6.11±0.03	6.14±0.03	6.13±0.03	6.06±0.02

References

- Arnaud, M., & Raymond, J. 1992, ApJ, 398, 394
- Aschwanden, M. J., *et al.* 1995, in preparation
- Behring, W. E., Cohen, L., Feldman, U., & Doschek, G. A. 1976, ApJ, 203, 521
- Brickhouse, N. S., Raymond, J. C., & Smith, B. W. 1995, ApJS, in press
- Brosius, J. W., Davila, J. M., Thomas, R. J., & Thomspen, W. T. 1994, ApJ, 425, 343
- Brosius, J. W., Davila, J. M., Thompson, W. T., Thomas, R. J., Holman, G. D., Gopalswamy, N., White, S. M., Kundu, M. R., & Jones, H. P. 1993, ApJ, 411, 410
- Brosius, J. W., Willson, R. F., Holman, G. D., & Schmelz, J. T. 1992, ApJ, 386, 347
- Davila, J. M., Thomas, R. J., Thompson, W. T., Keski-Kuha, R. A. M., & Neupert, W. M. 1993, UV and X-Ray Spectroscopy of Laboratory and Astrophysical Plasma, ed. E. Silver, S. Kahn (Cambridge: Cambridge), 301
- Doschek, G. A. 1984, ApJ, 279, 446
- Dupree, A. K., Huber, M. C. E., Noyes, R. W., Parkinson, W. H., Reeves, E. M., & Withbroe, G. L. 1973, ApJ, 182, 321
- Falconer, D. A. 1994, PhD Thesis, University of Maryland
- Falconer, D. A., Davila, J. M., & Thomas, R. J. 1993, BAAS, 25, 1200
- Feldman, U. 1992, Physica Scripta, 46, 202
- Feldman, U., Mandelbaum, P., Seely, J. F., Doschek, G. A., & Gursky, H. 1992, ApJS, 81, 387
- Gary, D. E., & Hurford, G. J. 1994, ApJ, 420, 903
- Jones, H. P., Duvall, T. L., Jr., Harvey, J. W., Mahaffey, C. T., Schwitters, J. D., & Simmons, J. E. 1992, Sol. Phys., 139, 211
- Keski-Kuha, R. A. M., Thomas, R. J., & Davila, J. M. 1992, Proc. SPIE, 1546, 614
- Klimchuk, J. A., & Gary, D. E. 1995, ApJ, in press
- Landini, M., & Monsignori-Fossi, B. C. 1993, A&A, 275, L17
- Mango, S. A., Bohlin, J. D., Glackin, D. L., & Linsky, J. L. 1978, ApJ, 220, 683

- Meyer, J.-P. 1993, *Adv. Space Res.*, vol. 13, no. 9, p. 377
- Monsignori-Fossi, B. C., & Landini, M. 1991, in "Intensity Integral Inversion Techniques: a Study in Preparation for the SOHO Mission," ed. R. A. Harrison & A. M. Thompson, RAL-91-092, p. 27
- Monsignori-Fossi, B. C., & Landini, M. 1994a, *A&A*, 284, 900
- Monsignori-Fossi, B. C., & Landini, M. 1994b, *Sol. Phys.*, 152, 81
- Monsignori-Fossi, B. C., & Landini, M. 1995a, in preparation
- Monsignori-Fossi, B. C., & Landini, M. 1995b, in *Proc. IAU Col. 152*, eds. S. Bowyer, B. Haisch, in press
- Monsignori-Fossi, B. C., Landini, M., Fruscione, A., & Dupuis, J. 1995a, *ApJ*, in press
- Monsignori-Fossi, B. C., Landini, M., Drake, J. J., & Cully, S. L. 1995b, *A&A*, in press
- Neupert, W. M., Brosius, J. W., Thomas, R. J., & Thompson, W. T. 1992a, *ApJ*, 392, L95
- Neupert, W. M., Epstein, G. L., Thomas, R. J., & Thompson, W. T. 1992b, *Sol. Phys.*, 137, 87
- Neupert, W. M., & Kastner, S. O. 1983, *A&A*, 128, 188
- Nitta, N., White, S. M., Kundu, M. R., Gopalswamy, N., Holman, G. D., Brosius, J. W., Schmelz, J. T., Saba, J. L. R., & Strong, K. T. 1991, *ApJ*, 374, 374
- Saba, J. L. R., & Strong, K. T. 1991, *ApJ*, 375, 789
- Saba, J. L. R., & Strong, K. T. 1993, *BAAS*, 25, 1201
- Schmelz, J. T., Holman, G. D., Brosius, J. W., & Gonzalez, R. D. 1992, *ApJ*, 399, 733
- Schmelz, J. T., Holman, G. D., Brosius, J. W., & Willson, R. F. 1994, *ApJ*, 434, 786
- Schmelz, J. T., Strong, K. T., & Lemen, J. R. 1993, *BAAS*, 25, 1201
- Thomas, R. J., Keski-Kuha, R. A. M., Neupert, W. M., Condor, C. E., & Gum, J. S. 1991, *Appl. Opt.*, 30, 2245
- Thomas, R. J., & Neupert, W. M. 1994, *ApJS*, 91, 461
- Thompson, W. T., Neupert, W. M., Jordan, S. D., Jones, H. P., Thomas, R. J., & Schmieder, B. 1993, *Sol. Phys.*, 147, 29

Tsuneta, S., *et al.* 1991, Sol.Phys., 136, 37

Vernazza, J. E., & Reeves, E. M. 1978, ApJS, 37, 485

Widing, K. G., & Feldman, U. 1993, BAAS, 25, 1201

Young, P. R., & Mason, H. E. 1995, private communication

Young, P. R., Mason, H. E., & Thomas, R. J. 1995, in Proc. 3rd SOHO Workshop, ESA SP-no.

Figure Captions

Figure 1. Background-corrected spectrum of AR 7563, obtained from a 99.4 s exposure and averaged along a 163'' slit segment, acquired during the SERTS flight of 1993 August 17. The x-axis gives the wavelength in \AA , and the y-axis gives the spectral intensity in $\text{ergs cm}^{-2} \text{s}^{-1} \text{sr}^{-1} \text{\AA}^{-1}$.

Figure 2. Background-corrected spectrum of quiet Sun area, obtained from a 202.3 s exposure and averaged along a 282'' slit segment, acquired during the SERTS flight of 1993 August 17. The x-axis gives the wavelength in \AA , and the y-axis gives the spectral intensity in $\text{ergs cm}^{-2} \text{s}^{-1} \text{sr}^{-1} \text{\AA}^{-1}$.

Figure 3. Background-corrected spectrum of AR 6615, obtained from a 202.3 s exposure and averaged along a 159'' slit segment, acquired during the SERTS flight of 1991 May 7. The x-axis gives the wavelength in \AA , and the y-axis gives the spectral intensity in $\text{ergs cm}^{-2} \text{s}^{-1} \text{sr}^{-1} \text{\AA}^{-1}$.

Figure 4. Background-corrected spectrum of quiet Sun area, obtained from a 99.4 s exposure and averaged along a 132'' slit segment, acquired during the SERTS flight of 1991 May 7. The x-axis gives the wavelength in \AA , and the y-axis gives the spectral intensity in $\text{ergs cm}^{-2} \text{s}^{-1} \text{sr}^{-1} \text{\AA}^{-1}$.

Figure 5. Background-corrected spectrum of off-limb area, obtained from a 99.4 s exposure and averaged along a 53'' slit segment, acquired during the SERTS flight of 1991 May 7. The x-axis gives the wavelength in \AA , and the y-axis gives the spectral intensity in $\text{ergs cm}^{-2} \text{s}^{-1} \text{sr}^{-1} \text{\AA}^{-1}$.

Figure 6. Plot showing the average active region over quiet Sun line intensity ratio, as a function of iron ionization stage, for the 1993 (asterisks) and 1991 (boxes) SERTS flights.

Figure 7. Active region differential emission measure curves derived from (a) 1993 and (b) 1991 observations. The x-axis gives the log of the temperature in K, and the y-axis gives the log of the DEM in $\text{cm}^{-5} \text{K}^{-1}$.

Figure 8. Quiet Sun differential emission measure curves derived from (a) 1993 and (b) 1991 observations. The x-axis gives the log of the temperature in K, and the y-axis gives the log of the DEM in $\text{cm}^{-5} \text{K}^{-1}$.

Figure 1

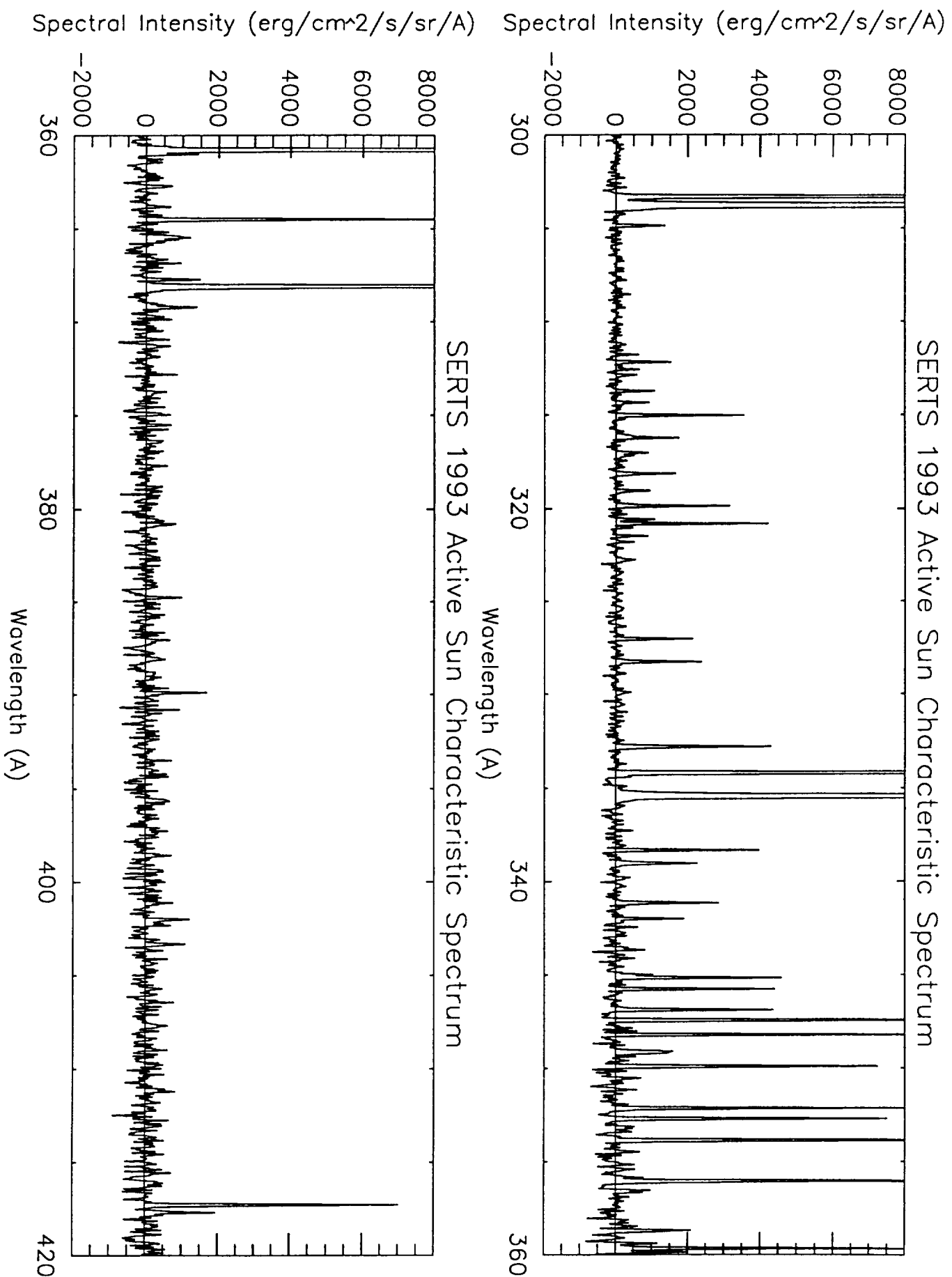


Fig 1

Figure 2

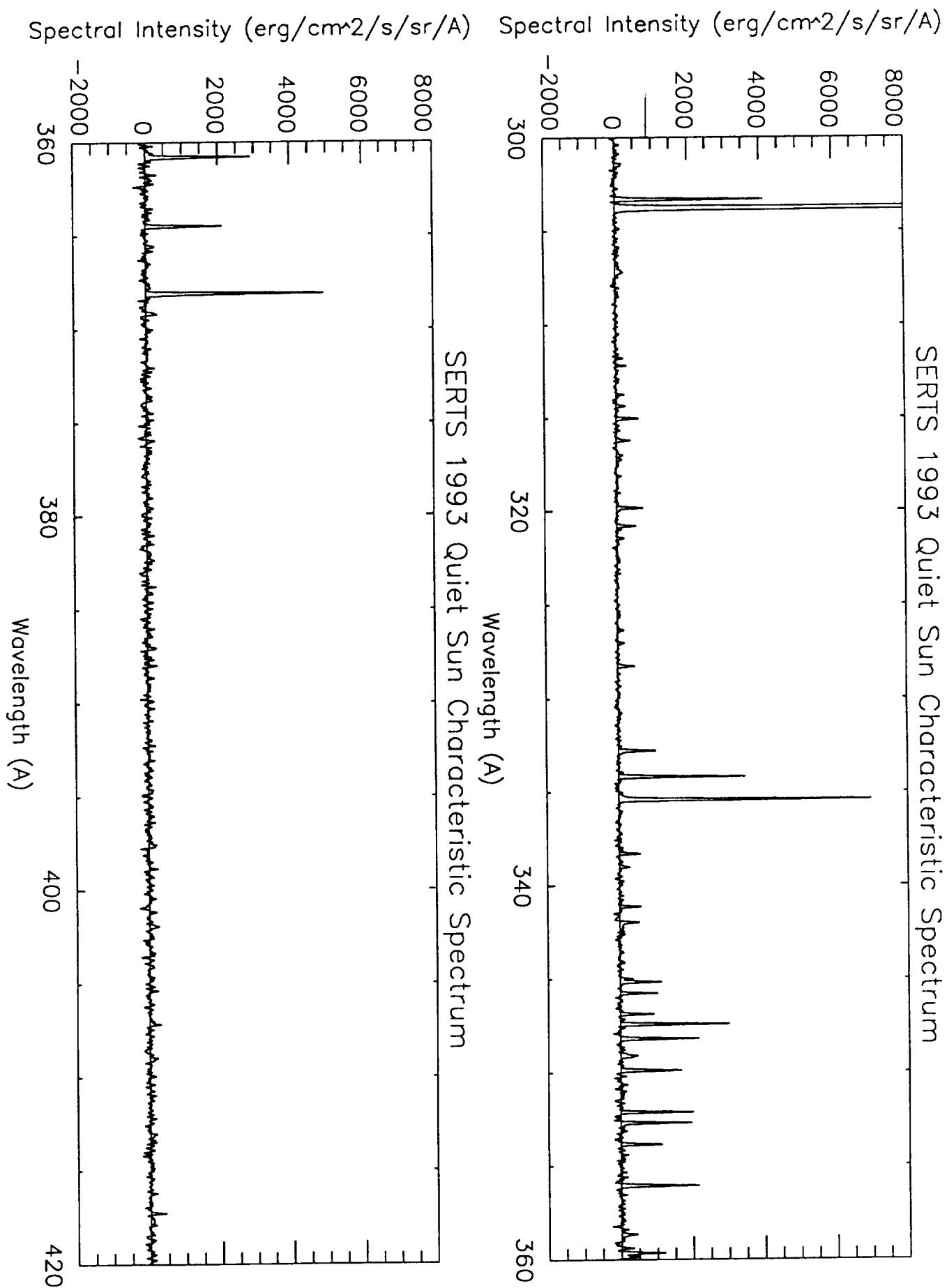


Fig 2

Figure 3

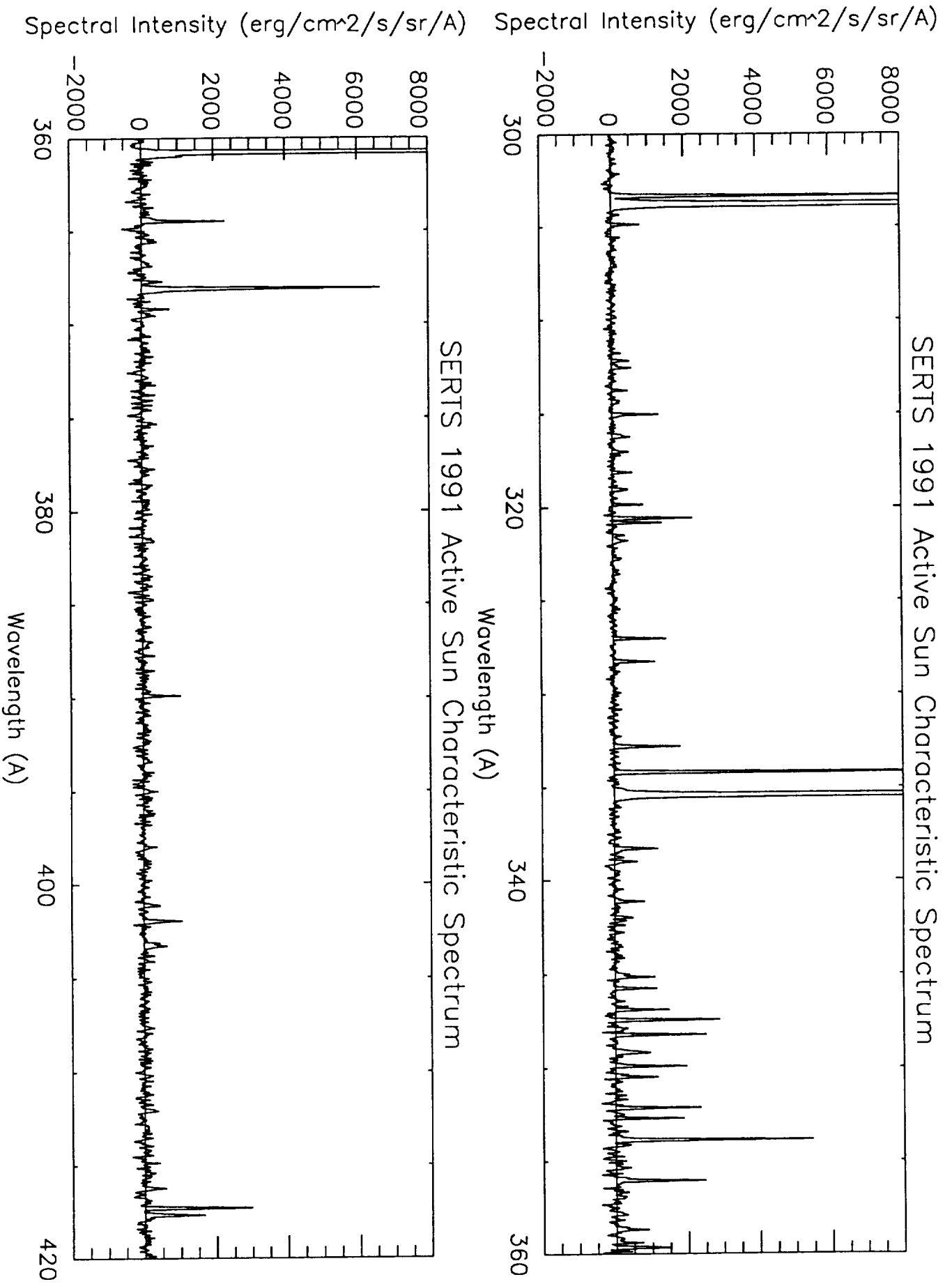


Fig 3

Figure 4

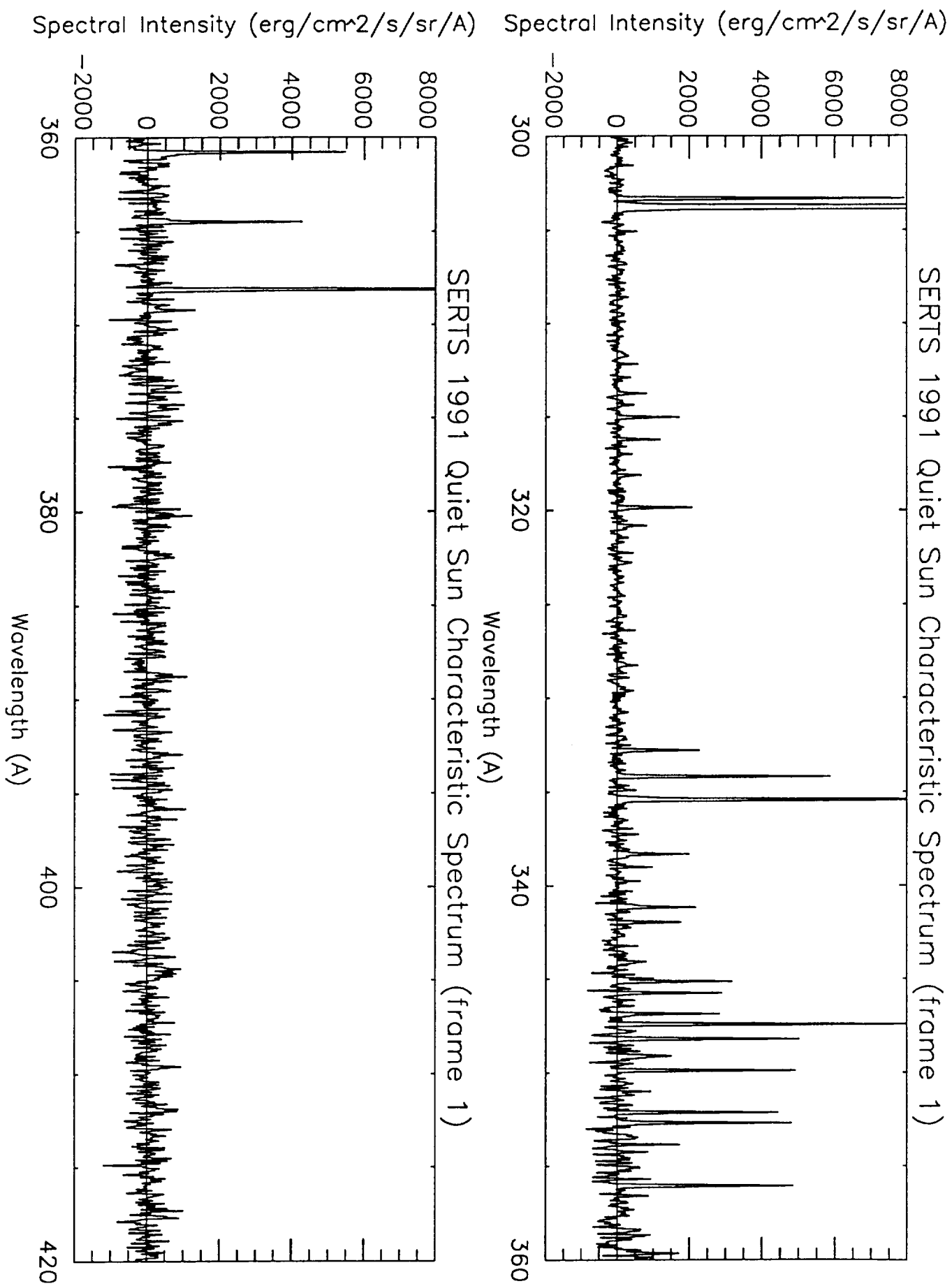


Fig 4

Figure 5

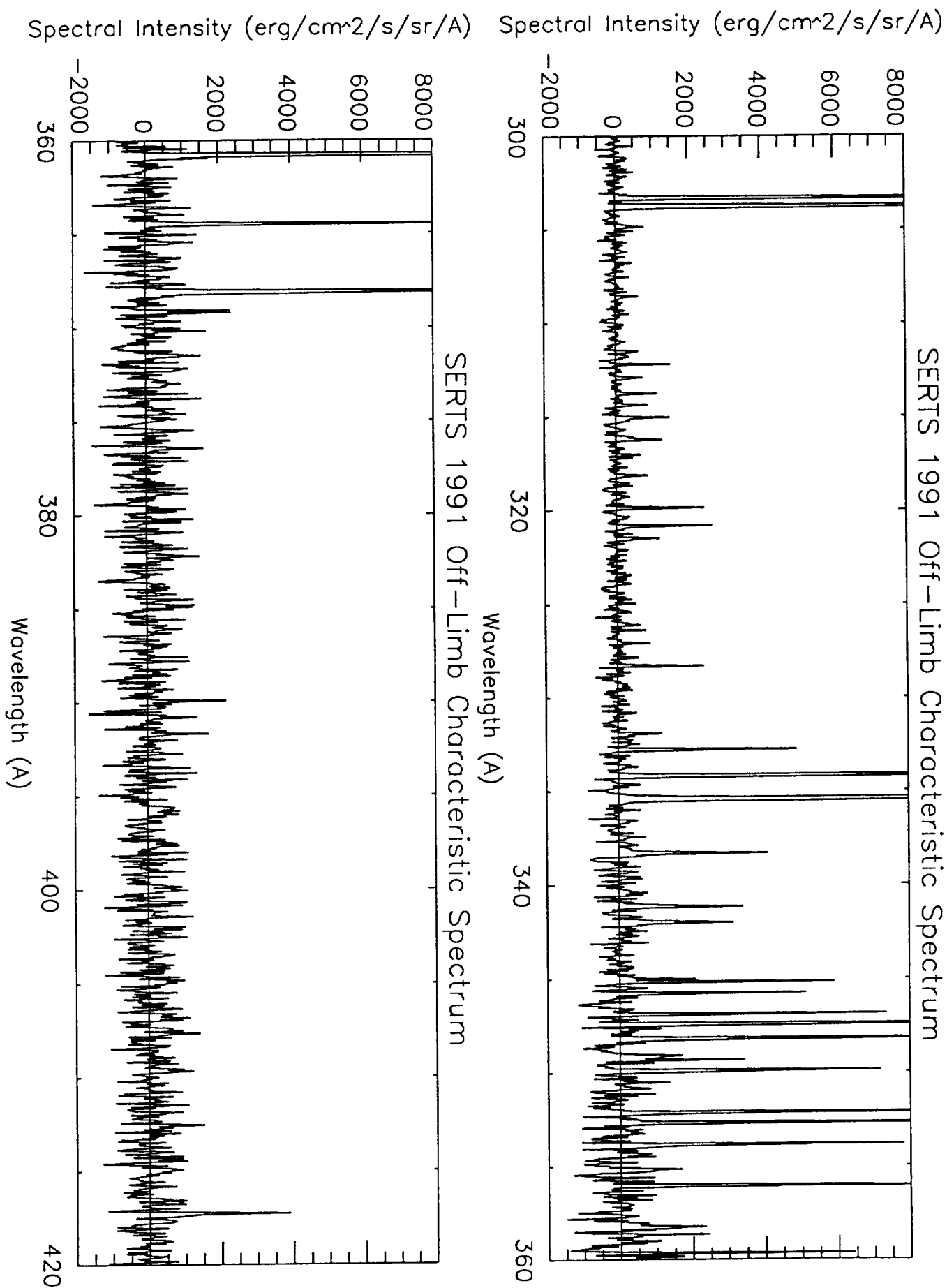


Fig 5

Fig. 6

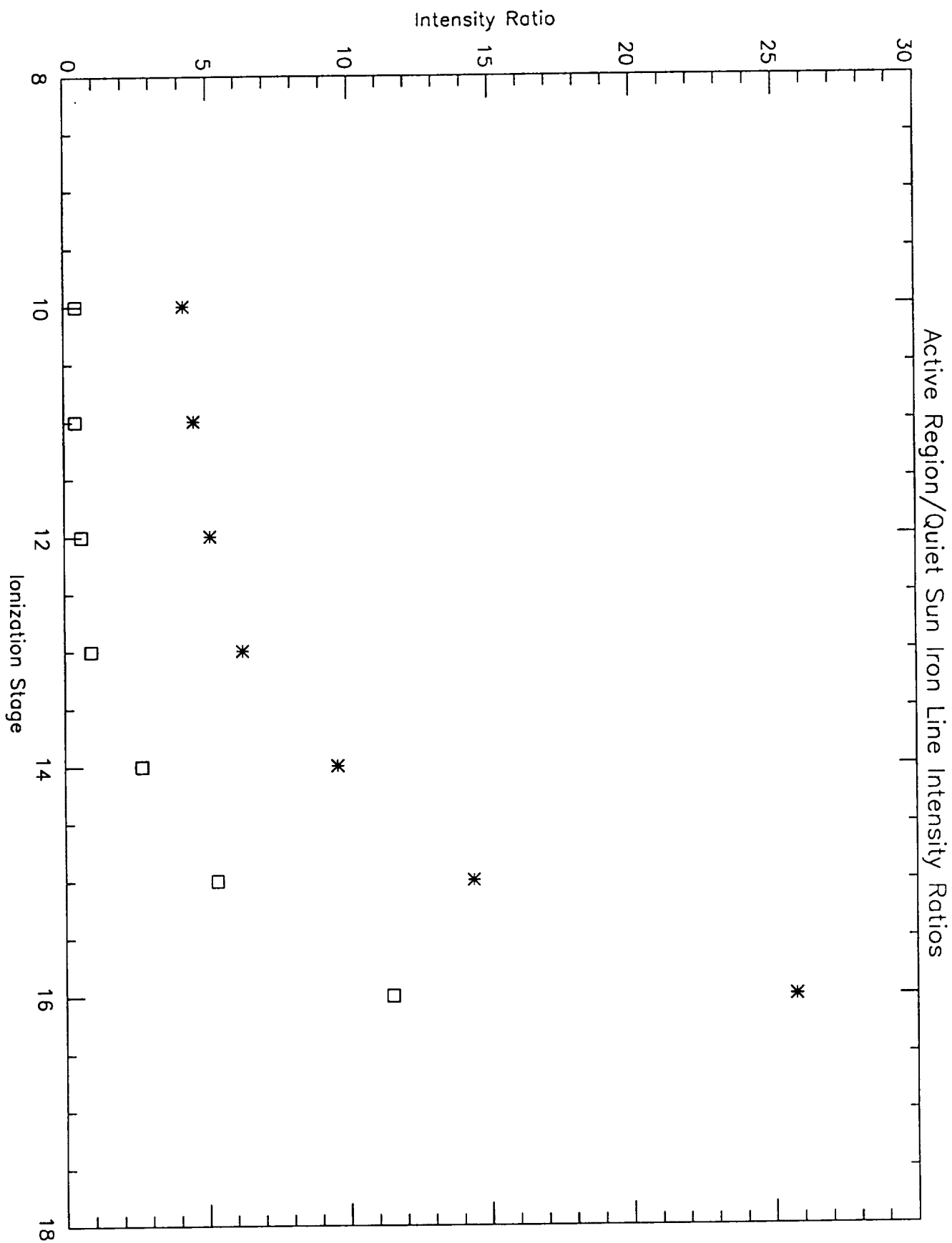


Fig 4

Fig. 7a

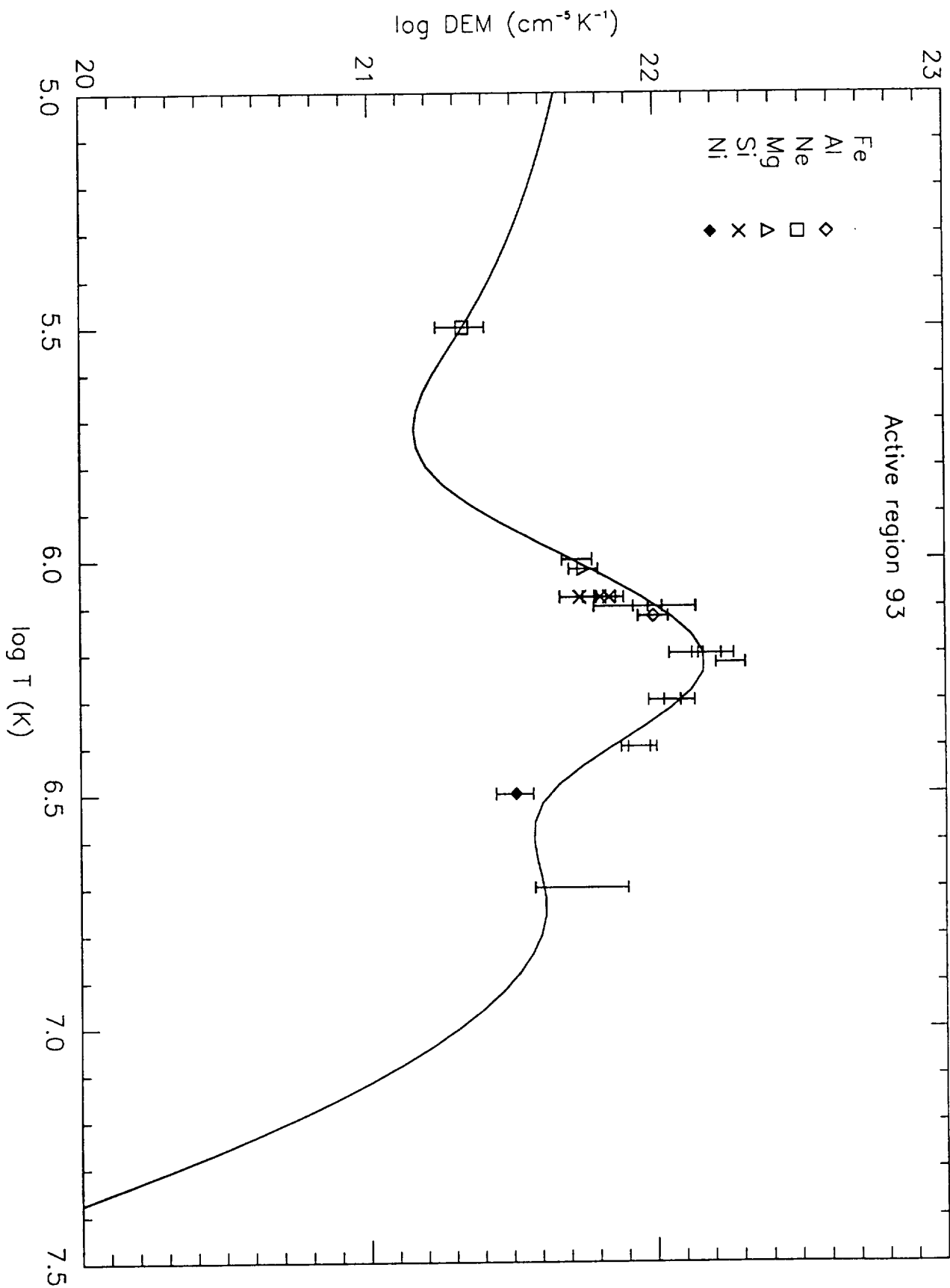


Fig 7a

Fig. 7b

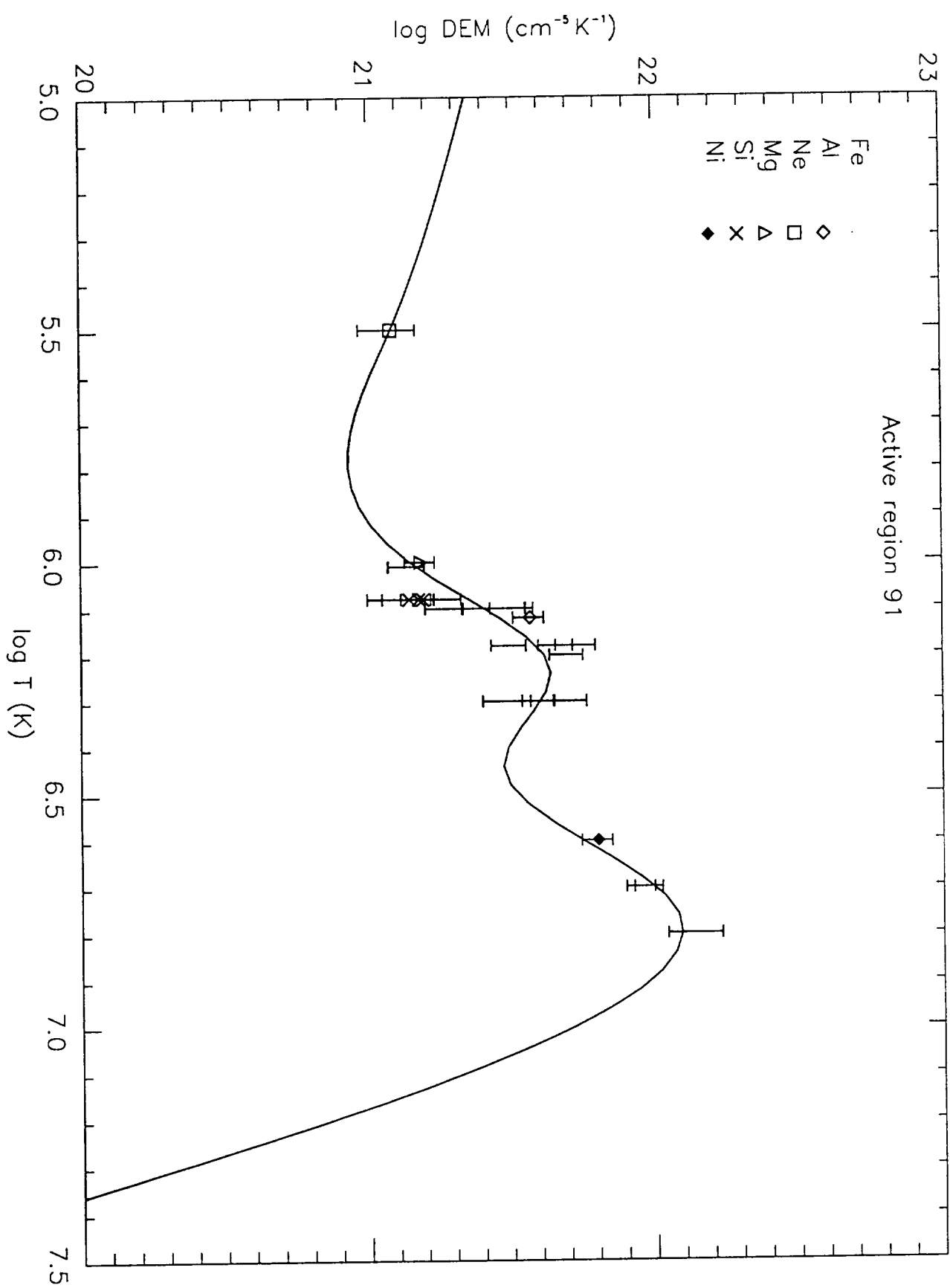


Fig 7b

Fig. 8a

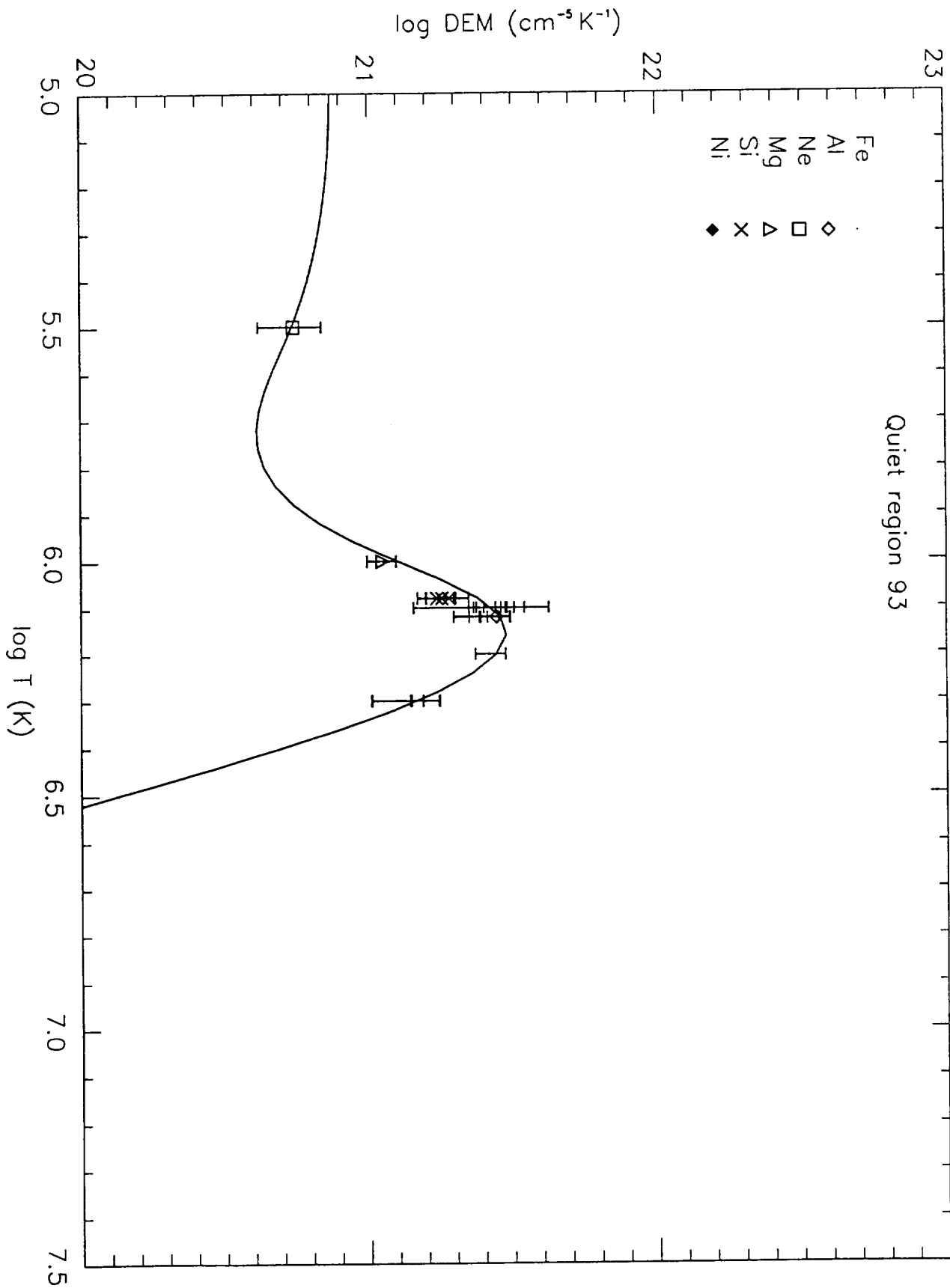


FIG 8A.

Fig. 8b

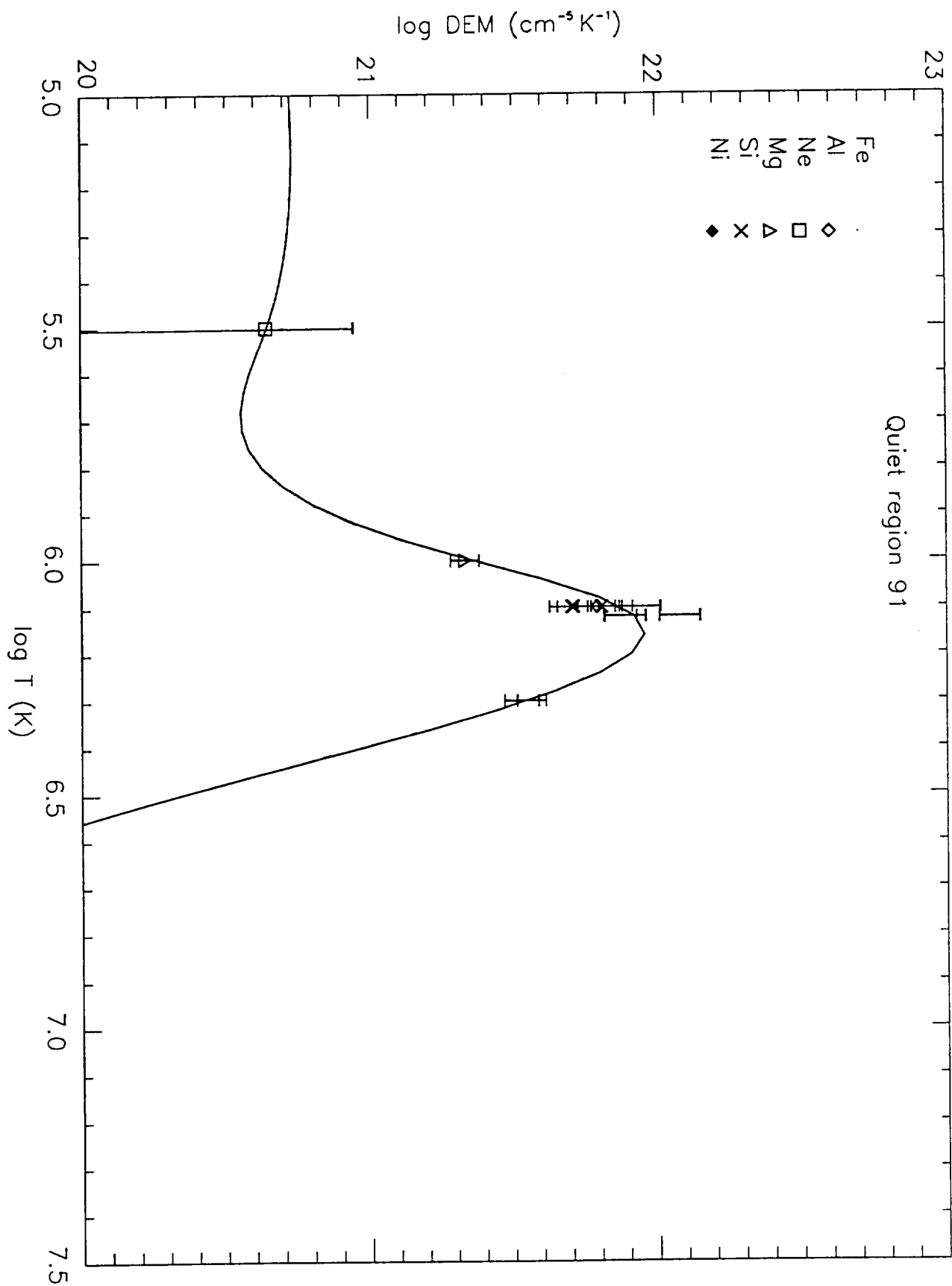


Fig 8b